PLASMON ENHANCEMENT OF MN^{2+} LUMINESCENCE AND APPLICATION OF TEMPERATURE-DEPENDENT MN^{2+} LUMINESCENCE

A Dissertation

by

YEROK PARK

Submitted to the Office of Graduate and Professional Studies of
Texas A&M University
in partial fulfillment of the requirements for the degree of

DOCTOR OF PHILOSOPHY

Chair of Committee,	Dong Hee Son
Committee Members,	James Batteas
	Christian Hilty
	Arum Han
Head of Department,	Francois Gabbai

December 2014

Major Subject: Chemistry

ABSTRACT

Doping semiconductor nanocrystals, commonly known as quantum dots (QDs), has attracted significant attention from the scientific community due to the highly tunable nature of the physical properties, such as optical, electrical, opto-magnetic properties, with respect to both size and dopant type/concentration. In this dissertation, Mn-doped CdS/ZnS (core/shell) QDs were used as a model system to study the characteristics of dopant luminescence coupled with plasmonic metal nanoparticles (MNPs) and its application as a nano-thermometer using temperature dependent Mn luminescence.

In the first part of this dissertation, plasmon-enhanced Mn luminescence from the Mn-doped CdS/ZnS QDs near plasmonic MNPs was studied. Rapid intraparticle energy transfer between exciton and Mn, occurring on a few picoseconds time scale, separates the absorber (exciton) from the emitter (Mn), whose emission is detuned far from the plasmonic absorption of the MNP. The rapid temporal separation of the absorber and emitter combined with the reduced spectral overlap between Mn and plasmonic MNP suppresses the quenching of the luminescence while taking advantage of the plasmon-enhanced excitation. The plasmon enhancement of exciton and Mn luminescence intensities in undoped and doped QDs were simultaneously compared as a function of the distance between MNP and QD layers in a multilayer structure to examine the expected advantage of the reduced quenching in the sensitized luminescence. At the optimum MNP-QD layer distance, Mn luminescence exhibits stronger net enhancement

(ca. twice) than that of the exciton, which can be explained with a model incorporating fast sensitization along with reduced emitter-MNP spectral overlap.

In the second part, ratiometric thermometry on Mn luminescence spectrum was performed using Mn-doped CdS/ZnS core/shell QDs that have a large local lattice strain on Mn site, which results in the enhanced temperature dependence of the bandwidth and peak position. Mn luminescence spectral lineshape is highly robust with respect to the change in the polarity, phase and pH of the surrounding medium and aggregation of the QDs, showing great potential in temperature imaging under chemically heterogeneous environment. The temperature sensitivity ($\Delta I_R/I_R$ = 0.5%/K at 293 K, I_R = intensity ratio at two different wavelengths) is highly linear in a wide range of temperatures from cryogenic to above-ambient temperatures. Surface temperature imaging was demonstrated on a cryo-cooling device showing the temperature variation of ~200 K (77–260 K) by imaging the luminescence of the QD film formed by simple spin coating, taking advantage of the environment-insensitive luminescence.

DEDICATION

To my beloved Hyunhee, Yulbin, and Subin

ACKNOWLEDGEMENTS

It is been a long and harsh journey for me to get to the point, and I have received help from many people whom I really appreciate and would like to acknowledge as I complete this dissertation and my PhD degree. First of all, I would like to thank my advisor, Dr. Son, for his excellent guidance and advising. As an advisor, he has been thoughtful, caring, and patient, serving as an invaluable source of knowledge and creativity. I credit him with opening my eyes to the way of scientific research, and helping me to understand how to conceptualize, elaborate, and distill my scientific thought. With his profound help, I believe I have gradually become a scientist, even though there are still many things to learn. Moreover, his passion for science always encourages me to be motivated and to immerse myself completely in my research.

I would also like to express my appreciation to my committee members, Dr. Batteas, Dr. Hilty, Dr. Han, Dr. Banerjee and a previous member, Dr. Cheng who is now a faculty member at South University of Science and Technology of China. It was great honor for me to collaborate with all the committee members' group. Even though results from some projects did not give rise to publication, all the projects provided good chances for me to test scientific ideas, develop experimental techniques, and increase/expand my scientific knowledge. I also want to express my appreciation to my old advisor, Prof. Sung giving me opportunity to continue my work on the TFT-memory project while I had a hard time in 2011.

All my current and previous group members deserve to have my thanks. Hsiang-Yun was a good friend and senior student who helped me a lot when I first started research in Dr. Son's lab. Daniel, Yitong, and Ho are good colleagues to discuss research topics and also good friends to chat about personal and interesting issues whenever I want to refresh myself. I also am grateful for previous members, Tai-Yen, Chih-Hao, Stacey, and Sourav.

Finally, a special thanks to my beloved wife, Hyunhee, two cute daughters, Yulbin and Subin, and all my other family members. From the deepest part of my heart, I would like to appreciate my wife Hyunhee's sacrifice for my studies. I will not forget any sacrifice and support from all my family members. I am blessed to have made it through this hard time with my family.

NOMENCLATURE

α	Electronic polarizability
Γ_E	Excitation rate
Γ'_E	Plasmon-modified excitation rate
ΔOD	Difference of optical density
$\mathsf{E}_a(\lambda)$	Molar extinction spectrum of Ag nanoparticles
ε_m	Dielectric constant of a surrounding medium
ε_s	Complex dielectric constant of metal nanoparticle
ρ_e	Density of excited states of a luminophore
τ_{avg}	Average lifetimes
Φ_{Col}	Light collection efficiency of an optical measurement system
Φ_{In}	Electric potential inside a metal nanoparticle
Φ_{Out}	Electric potential outside a metal nanoparticle
Φ_{PL}	Photoluminecence Quantum efficiency
Φ'_{PL}	Plasmon-modified quantum efficiency in photoluminescence of a luminophore
ω	Frequency of vibrational mode coupled to the Mn^{2+} ligand-field transition
AFM	Atomic force microscope
APTES	(3-aminopropyl)triethoxysilane
CCD	Charge-coupled device

E_{Max}	Peak maximum of Mn luminescence lineshape in photon energy
$\mathbf{E_0}$	Applied electric field of incident light
$\mathbf{E_{Out}}$	Electric field outside a metal nanoparticle
EPR	Electron paramagnetic resonance
$F_d(\lambda)$	Normalized luminescence spectrum of donor
FEM	Finite element method
FRET	Förster resonance energy transfer
I	Photoluminescence intensity of a luminophore
I'	Plasmon-modified photoluminescence intensity of a luminophore
I_{Mn}	Mn photoluminescence intensity
I'_{Mn}	Plasmon-modified Mn photoluminescence intensity
ICP-MS	Inductively coupled plasma mass spectrometry
J	Spectral overlap integral
k_{ET}	Energy transfer rate from an exciton to Mn^{2+} ions
k'_{ET}	Energy transfer rate from an excited luminophore to an adjacent metal nanoparticle
k_{nr}	Nonradiative rate constant
$k_{nr,ex}$	Nonradiative rate constant for exciton luminescence
$k_{nr,Mn}$	Nonradiative rate constant for Mn luminescence
$k_{Q,ex}$	Rate constant for exciton luminescence via exciton-metal nanoparticle energy transfer
$k_{Q,Mn}$	Rate constant for Mn luminescence via Mn-metal

	nanoparticle energy transfer
k_r	Radiative rate constant
$k_{r,ex}$	Radiative rate constant for exciton luminescence
$k_{r,Mn}$	Radiative rate constant for Mn luminescence
LSP	Localized surface plasmon
MNP	Metal nanoparticle
MO	Molecular orbital
NCs	Nanocrystals
n_E	Distance dependence power for plasmon-enhanced luminescence
n_Q	Distance dependence power for plasmon-quenched luminescence
ODE	1-Octadecene
OAm	Oleylamine
OD	Optical density
P_E	Excitation enhancement factor for a luminophore
	induced by metal nanoparticles
P_Q	Quenching factor for a luminophore induced
	by metal nanoparticles
$\mathbf{P_T}$	Transition dipole moment of an optical species
PDMS	Polydimethylsiloxane
Pdots	Polymer dots
PL	Photoluminescence
QDs	Quantum dots

QY_{ET}	Quantum yield for exciton-Mn energy transfer
R_Q	Length at which half the luminescence is quenched
R_E	Length at which the luminescence enhancement by a factor of two
RhB	Rhoamine B
RT	Room temperature
SILAR	Successive Ionic Layer Adsorption and Reaction
TCSPC	Time-correlated single photon counting
TEM	Transmission electron microscopy
THF	Tetrahydrofuran

TABLE OF CONTENTS

Page

ABSTRACT ii

DEDICATION iv

ACKNOWLEDGEMENTS v

NOMENCLATURE vii

TABLE OF CONTENTS xi

LIST OF FIGURES xiv

LIST OF TABLES xvii

CHAPTER

I INTRODUCTION 1

II BACKGROUND AND LITERATURE OVERVIEW 7

2.1 Mn-Doped II-VI Semiconductor Nanocrystals……..… 7
2.1.1 Synthesis of Mn-Doped II-VI Semiconductor Nanocrystals 7
2.1.2 Electronic Structure of Mn-Doped II-VI Semiconductor Nanocrystals 9
2.1.3 Dynamic Processes in Phtoexcited Mn-Doped II-VI Semiconductor Nanocrystals……..... 11
2.1.4 Optical Properties in Mn-Doped II-VI Semiconductor Nanocrystals…… 13
2. 2 Plasmon-Controlled Luminescence…..…… 15
2.2.1 Optical Properties of the Plasmonic Metal Nanoparticles…..... 15
2.2.2 Plasmon- Modified Luminescence of Typical Luminophores……..... 18
2.2.3 Plasmon-Modified Luminescence of Mn-Doped Semiconductor Nanocrystals……..... 21

CHAPTER Page

2.3 Luminescence Nanothermometry……. 22
2.3.1 Ratiometric Luminescence Nanothermometry…..… 22
2.3.2 Tuning Temperature-Dependent Mn Luminescence.. 25

III SYNTHESIS OF MN-DOPED CDS/ZNS CORE/SHELL QUANTUM DODTS AND EXPERIMENTAL METHODS 29

3.1 Synthesis of Mn-Doped and Undoped CdS/ZnS Core/Shell Quantum Dots…… .. 29
3.1.1 Synthesis of Undoped CdS/ZnS Core/Shell Quantum Dots.. 29
3.1.2 Synthesis of Mn-doped CdS/ZnS Core/Shell Quantum Dots and Water-Soluble Ligand Exchange. 30
3.2 Determination of the Doping Concentration……..... 32
3.3 Measurement of Time-Dependent Mn and Exciton Luminescence Intensity……... 33
3.4 Fabrication and Characterization of the Multilayered Structure on the Ag MNP-Patterned Substrate…….. .. 33
3.5 Imaging of Plasmon-Enhanced Luminescence Intensity on the Patterned Structure……..… 35
3.6 Measurement of the Temperature-Dependent Mn Luminescence Spectra……... 36
3.7 Fabrication and Surface Temperature Imaging of Cryo-Cooling Device……..... 36

IV SUPPRESION OF QUENCHING IN PLASMON-ENHANCED LUMINESCENCE VIA RAPID INTRAPARTICLE ENERGY TRANSFER IN DOPED QUANTUM DOTS…….. 39

4.1 Introduction 39
4.2 Results and Discussion..... 41
4.3 Conclusions 54
4.4 Experimental Section 55
4.4.1 Materials Used for Synthesis of Quantum Dots……. 55
4.4.2 Synthesis of the Mn-Doped and Undoped CdS/ZnS Core/Shell Quantum Dots……..... 55
4.4.3 Fabrication and Characterization of the Multilayered Structure on the Ag MNP-Patterned Substrate…… .. 58
4.4.4 Measurements of Spacer Layer Thickness and Distribution of QD-Ag MNP Inter-Particle Distances Distribution……..…... 59

CHAPTER Page

4.4.5 Imaging of Plasmon-Enhanced Luminescence Intensity on the Patterned Structure…… 61
4.4.6 Time-Resolved Luminescence Intensity Measurements……..…..... 62
4.4.7 Comparison of the Time-Resolved Luminescence Intensity between the Dilute Solution and the Thin Film Sample… 63
4.4.8 Test of the Effect of the Multilayered Structure (Polyelectrolyte Layer/Ag MNP/APTES/Si Substrate) on the Collection Efficiency at Different Wavelengths 64
4.4.9 Modeling *d*-Dependence of Plasmon-Enhanced Luminescence..... 65

V RATIOMETRIC TEMPERATURE IMAGING USING ENVIRONMENT-INSENSITIVE LUMINESCENCE OF MN-DOPED CORE/SHELL NANOCRYSTALS…….. 68

5.1 Introduction 68
5.2 Results and Discussion..... 71
5.3 Conclusions 81
5.4 Experimental Section 82
5.4.1 Synthesis of Mn-Doped CdZ/ZnS Core/Shell Nanocrystals with Controlled Radial Doping Location……..... 82
5.4.2 Measurement of the Temperature-Dependent Mn Luminescence Spectra……. 83
5.4.3 Cryo-Cooling Device Fabrication…… 83
5.4.4 Surface Temperature Imaging of the Cyro-Cooling Device……... 83
5.4.5 Finite Element Method Simulation 85

VI SUMMARY…….. 87

REFERENCES…….. 90

LIST OF FIGURES

FIGURE		Page
II-1	(a)Zinc blende crystal structure of Mn-doped II-VI nanocrystals. (b) Electronic configuration of the lowest excited state ($^4T_1$) and ground state ($^6A_1$) of Mn2+ ions in tetrahedral sites. (c) Comparison between the lowest excited energy state of Mn^{2+} ions in the ligand field and bulk band gaps of typical II-VI semiconductor nanocrystals……..	10
II-2	(a) Extinction and physical cross sections of different kinds of optical species. (b) Ratio between the extinction and physical cross sections versus physical sizes of the optical species. Figure adapted from Ming's work.[29].	16
II-3	(a) A schematic of Mn-doped CdS/ZnS core/shell QDs with radial doping location (d) of Mn^{2+} ion (yellow small dot). (b) Calculated strain of CdS/ZnS core/shell QDs with size of core radius (1.8nm) and shell thickness (1.8nm). Figure adapted from Chen's work.[26]	26
IV-1	(a) Multilayer structure fabricated on Si substrate used for the comparison of plasmon-enhancement of exciton and Mn luminescence. (b) AFM image of the patterned Ag MNP layer on Si substrate before adding spacer and QD layer	42
IV-2	Comparison of the absorption (solid lines) and luminescence (dashed lines) spectra of the Mn-doped (red) and the undoped (blue) CdS/ZnS QDs. Extinction spectrum of the Ag MNPs is shown in black solid line. The QD luminescence and Ag MNP extinction spectra are normalized.	43
IV-3	False-color images of Mn luminescence from the multilayered structure shown in Figure 1 with spacer layer thickness of 3 nm (a) and 9 nm (b). The bottom panels show the line profile of the intensity ratio (I/I_0) for Mn (red) and exciton (blue) luminescence at the region indicated with white dashed lines vertically averaged over 20 μm. (c) I/I_0 for exciton and Mn luminescence at different spacer layer thicknesses (t).	44
IV-4	(a) Kinetic scheme of the photophysical processes in Mn-doped QD adjacent to Ag MNP. (b) d-dependence of QY_{ET} (dashed), $P_{Q,Mn}$ (red) and $P_{Q,ex}$ (blue) in Eq. 1 and 2. See the text for the parameters used for this plot. (c) d-dependence of I/I_0 for Mn (red) and exciton (blue)	

FIGURE Page

luminescence calculated from Eq. 1 and 2 using the same set of parameters used in (b). 49

IV-5 Time-resolved (a) Mn and (b) exciton luminescence intensity at various polymer spacer layer thicknesses…….. .. 51

IV-6 TEM images of the undoped and the Mn-doped CdS/ZnS QDs. Magnification is (a) 100k and (b) 250k of the undoped QDs, and (c) 100k and (d) 250k of the Mn-doped QDs…… 57

IV-7 TEM image of the Ag nanoparticles…… 57

IV-8 AFM images of the Si substrate with the patterned Ag MNPs (a) 9×9 μm^2, (b) 1×1 μm^2 area……. 60

IV-9 The height profile of the polymer spacer layers on the scratched Si substrate measured with tapping-mode AFM……. 61

IV-10 Calculated distribution of center-to-center distances between QD and Ag MNP……... 61

IV-11 Optical setup for the imaging of luminescence…… 62

IV-12 Time-resolved (a) Mn and (b) exciton luminescence intensity from the dilute solution and the dropcast thin film sample…… 64

IV-13 Images of scattered/reflected light projected on the same construct (polyelectrolytes/with or without Ag NPs/APTES/Si substrate) at two different wavelengths (450 and 600 nm), (a) with Ag NPs at 450 nm ($I_{layer,450}$), (b) without Ag NPs at 450 nm ($I_{bare,450}$), (c) with Ag NPs at 600 nm ($I_{layer,600}$), (d) without Ag NPs at 600 nm ($I_{bare,600}$). (e) The region of interest (red dotted line shown in (a)) in the ratio image of ($I_{layer,450}/I_{bare,450}$)/ ($I_{layer,600}/I_{bare,600}$) and (f) the cross section in (e) (blue solid line)……. 65

V-1 (a) Normalized Mn luminescence spectra of Mn-doped (at the interface between the CdS core and ZnS shell) NCs with high local lattice strain at Mn^{2+} sites used for thermometry in this study. (b) Intensity ratio of I_{600}/I_{650} at different temperatures (blue dots: experimental data, green line: interpolation curve). (c) Normalized Mn luminescence spectra of typical Mn-doped (in the ZnS shell) NCs with weak local lattice strain at Mn2+ ion sites. Insets in (a) and (c) pictorially represent the

structures of Mn-doped core/shell NCs with different radial doping locations……. . 72

V-2 Comparison of the normalized luminescence spectra of Mn-doped CdS/ZnS NCs under different medium environment. (a) Solvent dependence; chloroform (s_1) and water (s_2), (b) Medium phase dependence; on sapphire under vacuum (s_3), PMMA/sapphire (s_4), chloroform (s_1) is shown for comparison. (c) pH dependence: pH5 (s_5), pH7 (s_6) and pH9 (s_7). The bottom panels are the intensity difference of the normalized spectra. (a) s_1-s_2, (b) s_1-s_3 (blue), s_1-s_4 (red), (c) s_6-s_5 (blue), s_6-s_7 (red)…….. 76

V-3 (a) Schematics of the cryo-cooling device. The imaging area is indicated by the dashed rectangle. (b) Color contour plot of the intensity image (I_{650}) from the device with liquid nitrogen flow in the channel. (c) Color contour plot of the temperature converted from the intensity ratio image. (d) Temperature line profile (solid) and the simulation result (dashed) at the location indicated in (c)……. 78

V-4 The time-profile of the temperature of hexane solution of the NCs in a cuvette under the constant and varying temperature conditions. The temperature trace is converted from the luminescence intensity ratio shown in Figure 2(b)…… 80

V-5 Schematics of the cryo-cooling device, the enclosure and the temperature measurement setup. (a) The cryo-cooling device is in the enclosure in which dry nitrogen is constantly flushed. (b) The optical setup consists of filters (F), achromatic doublet lenses (L), and a dichroic mirror (M). The device was illuminated with a 365 nm LED and imaged with a CCD detector..... 84

LIST OF TABLES

TABLE Page

IV-1 Average luminescence lifetime of exciton (τ_{ex}) and Mn (τ_{Mn}) from the undoped and Mn-doped QDs respectively at varying spacer layer thicknesses (*t*)…….... 52

CHAPTER I

INTRODUCTION

Since a synthetic route for colloidal semiconductor nanocrystals was reported by Louis E. Brus et al. in early 1980s, colloidal semiconductor nanocrystals, known as quantum dots (QDs), have attracted considerable attention due to their unique and highly tunable optical, electrical, and magnetic properties.[1-5] Many of these intriguing properties are a result of the quantum confinement (or size) effect, which is attributed to the well-defined discrete energy levels in the nanocrystals, whose critical size is smaller than the exciton Bohr radius.[6,7] As the size of the semiconductor nanocrystals scales within the critical size, the bandgap of the semiconductor nanocrystals is tunable in UV/visible and even NIR region governed by the quantum confinement effect, which is the most prominent feature of the QDs.[7] The unprecedented size-tunable optical characteristic renders the semiconductor nanocrystals as one of the promising optical species in many applications such as light-emitting devices, biological imaging, solar cells, and nanothermometers.[8-14] Recently, electronics equipped with QD display have emerged in the commercial market to compete with the OLED displays, providing one of the first marketable real-world application of QD technology.[8]

As the optical, electrical, and magnetic properties of many semiconducting materials have been expanded with the addition of dopants, doped QDs have also attracted attention for introducing additional/supplementary optical, electrical, magneto-optical properties.[15-18] In order to meet those additional/supplementary properties, in the

past two decades many synthetic groups have made an effort to develop the various synthetic methods of the doped QDs.[19-22] While significant headway has been made towards the synthesis of stable QD's with controllable dopant density/location, there remains substantial challenges in these synthesis.[16] Doping methods for transition metals such as Cu or Mn ion have been widely developed to meet the need for eco-friendly QDs which are heavy metal-free emitters.[23,24] The representative doping methods can be categorized by synthetic approach such as 1) hot injection/cluster thermolysis, 2) nucleation-doping, and 3) layer-by-layer which are described in the Background section in detail.[19-22]

While the synthesis of doped QDs is an ongoing problem, characterization of these materials has subsequently offered a variety of interesting and difficult challenges. Many research groups in a variety of fields including physics, chemistry, and engineering, have directed their effort towards understanding the optical, electrical, and opto-magnetic properties in the doped QDs.[17,18,23,24] Understanding the optical properties of transition metal doped QDs and application for the dopant luminescence will be the main discussion in this dissertation. The unique optical properties of doped QDs are mainly attributed to the strong interaction (exchange coupling) between photo-generated excitons in the semiconductor matrix, and the transition metal dopant ions embedded in the matrix. Depending on the energetics of the exciton (donor) and dopant (acceptor) in the nanocrystals, fast exciton-dopant energy transfer due to such strong exchange coupling results in highly efficient photoluminescence quantum yield, competing over charge carrier trapping and nonradiative relaxation of exciton.[23,25] In this work, we

focused on Mn-doped CdS/ZnS core/shell QDs, which show highly efficient Mn (dopant) luminescence via fast energy transfer ($k_{ET} < 1 - 3 \times 10^{11} s^{-1}$) from the exciton to Mn^{2+} ion, compared to the electron/hole trapping of exciton ($k_{tr} > 1 - 2 \times 10^{10} s^{-1}$) .[23] Moreover, the Mn luminescence is highly photostable due to the localized nature of the dopant while the luminescence is not affected by variables in the surrounding environment. In addition, the development of the structural modification of the Mn-doped CdS/ZnS core/shell QDs can also make it possible to be utilized in the application field such as thermal sensing due to their significant temperature-dependent dopant luminescence via the optical tuning.[11,26] For these reasons, transition metal ion-doped QDs are considered as an important class of luminescent new nanomaterials.[24]

Consequently to the synthesis of semiconductor nanocrystals, the fabrication of noble metal nanocrystals has also attracted significant attention for their distinct optical property known as localized surface plasmon (LSP). A plasmon is the collective oscillation of conduction electrons against nuclear framework. Especially when the plasmon is confined in a small nanostructure comparable to the wavelength of incident light, it is referred to as LSP.[27,28] The plasmonic nanostructure can be used to manipulate the interaction between propagating far-field light and optical species at the nanometer scale, which gives rise to absorption or emission enhancement of the optical species.[29] Furthermore, control over the shape and size of the nanostructure can even manipulate direction and polarization of the light.[30,31] The unique ability of plasmonic nanostructure to manipulate the properties of light have resulted in the rapid expansion of fundamental and technological research into plasmonic nanosturtures in the field of photonics,

chemical/biological sensing, surface-enhanced raman spectroscopy, energy harvesting, and medical application.[32-35]

The plasmonic enhancement of the luminophore luminescence for many application purposes has been the focus of most LSPR research because the luminescence enhancement can increase the detection limit of the chemical/biological sensing or make more efficient light-emitting sources.[35,36] The luminescence enhancement is attributed to increase of excitation or emission rates by noble metal nanostructures in the vicinity of a luminophore, resulting from the enhanced local electric field by the LSP or the modification of the photonic mode adjacent to the plasmonic metal nanostructures.[27,29,37] Augmentation of excitation rate has been intensively studied especially with colloidal metal nanoparticles (MNPs) that exhibit strong plasmon resonance in the UV-vis and even near IR spectral region, in which many applications such as biological sensing/imaging, energy harvesting, and lighting devices are executed.[38-40] While the excitation rate of the luminophores can be augmented by the plasmon-enhanced local electric fields, at very short distances the luminescence can be quenched by the MNPs via luminophore-MNPs energy transfer which results from spectral overlap between luminophore's emission and the plasmonic MNPs' absorption.[41-44] The concurrent augmentation of the two opposing processes, i.e., excitation enhancement and emission quenching, is inevitable in most instances because of the comparatively wide plasmon resonance spectrum of the MNPs compared to the luminescence Stokes-shift of typical luminophores.[45] These two contradictory processes explain the strong dependence of the luminescence change on the MNP-luminophore

distance, which has been extensively studied to optimize the net plasmon-enhanced luminescence.[44,46,47]

In the first part of this dissertation, plasmon-enhanced Mn (dopant) luminescence was studied in Mn-doped CdS/ZnS core/shell QDs, which showed stronger net plasmon enhancement of the Mn luminescence with suppression of MNP-induced Mn luminescence quenching.[48] The net enhancement is attributed to the considerably large red-shifted dopant luminescence from both the exciton absorption and plasmon resonance spectrum of the MNPs. The remarkable red shift occurs because the Mn ligand-field transition energy (~2.10 eV) is much lower than the bandgap transition energy (~2.82 eV) of the exciton, which is the unique feature in the Mn-doped CdS/ZnS core/shell QDs.[23] It is demonstrated in the Mn-doped CdS/ZnS QDs which show sensitized Mn luminescence through rapid exciton-Mn energy transfer taking place on a few picoseconds time scale.[49,50] The rapid energy transfer from exciton to Mn^{2+} ions can separate the absorber (exciton) and emitter (Mn) and then decrease spectral overlap between the emitter and plasmon resonance (~3.1 eV) of the MNPs, resulting in the suppression of the quenching in the plasmon-enhanced luminescence.[48]

In the second part of this dissertation, the ratiometric thermal imaging method using the Mn-doped CdS/ZnS QDs as a luminescence nanothermometer was studied. Recent progress in the luminescence nanothermometry using temperature-dependent photoluminescence of organic dyes and nanocrystalline optical species made the thermal imaging possible with high accuracy (<0.1 °C) and spatial resolution (<10 μm).[11,51-62] The temperature dependent luminescence intensity, spectral position, bandwidth,

polarization and lifetime are the most frequently utilized thermal imaging mechanisms in the luminescence nanothermometry.[53-56] Even if the insensitivity of the temperature-dependent luminescence to the other variables except for the temperature is very important factor for the accurate and reliable thermal imaging method, the luminescence of many optical species utilized for the thermal imaging is often not only dependent on the temperature, but also affected by other factors such as polarity, phase or pH of the surrounding medium. [52,63-65] Therefore, insensitivity of the luminescence to the environmental conditions is important for accurate temperature sensing. In addition, for the luminescence intensity-based thermometry, the luminescence intensity itself can vary depending on the luminophore concentration and collection efficiency of the detection system. Therefore, ratiometric measurement of the multiple emitters has become more common recently, where the temperature-dependent ratio of the two different luminescence intensities is measured instead of the absolute intensity. [57-61]

The ratiometric thermal imaging method using the Mn-doped CdS/ZnS QDs is introduced to exhibit strong temperature dependence of the spectral lineshape while being insensitive to the surrounding chemical environment such as the polarity, phase and pH of the surrounding medium.[66] Control over Mn^{2+} ions doping location and concentration induces tunable local lattice strain at the dopant sites, which give rises to the enhanced temperature dependence on the bandwidth and peak position of the Mn luminescence. The surface temperature imaging was demonstrated on a cryo-cooling device, where the temperature sensitivity ($\Delta I_R/I_R$ = 0.5%/K at 293 K, I_R = intensity ratio at two different wavelengths) is highly linear in a wide range of temperatures (>200 K).

CHAPTER II

BACKGROUND AND LITERATURE OVERVIEW

2. 1 Mn-Doped II-VI Semiconductor Nanocrystals

2.1.1 Synthesis of Mn-Doped II-VI Semiconductor Nanocrystals

As the optical, electrical, and magnetic properties of many semiconducting materials have been expanded with the addition of dopants, doped semiconductor nanocrystlas, which is referred to as doped quantum dots (QDs), have also attracted attention for introducing additional optical, electrical, magneto-optical properties.[15-18] In order to meet those additional/supplementary properties, many synthetic groups have made an effort to develop the various synthetic methods of the doped QDs. [19-22] In 1994, Bhargava et al. reported the first colloidal doped QDs (Mn-doped ZnS).[67] The ZnS nanocrystals were synthesized by reacting diethylzinc and hydrogen sulfide gas in toluene, followed by addition of Mn precursor (diethyl-manganese) to the host nanocrystal solution at room temperature. Finally, the Mn-doped ZnS nanocrystals were coated with methacrylic acid to maintain the separation of the colloidal nanocrystals and increase the luminescence quantum yield. However, the synthesis method results in relatively low quality doped nanocrystals due to formation of defect sites in the host nanocrystals during the reaction at room temperature.

The next breakthrough in colloidal Mn-doped QDs was the synthesis of Mn-doped ZnSe introduced by Norris et al., reporting the high-quality Mn-doped ZnSe QDs showing 22% quantum yield using the thermolysis of organometallic precursors in a

coordinating solvent.[19] Precursors of Mn and other host elements were injected into the pre-heated coordinating solvent in the elevated temperature (>300 °C) to give rise to the Mn-doped ZnSe QDs. The high temperature provides thermal energy to anneal defects out of the nanocrystals.[68] However, the method still suffers from low doping yield and self-purification, which ejects the dopant ions onto the surface of host nanocrystals.[15,69]

To overcome low doping concentration and relatively low quantum yield of dopant luminescence, Peng et al. reported a new synthetic route named "Nucleation doping", in which MnSe clusters were nucleated and the host semiconductor was grown around the cluster at elevated temperatures, resulting in Mn-doped ZnSe QDs with about 50% luminescence quantum yield.[20] Since the host semiconductors were grown on the dopant clusters, the host nanocrystals were heavily doped. Furthermore, high concentration of the dopant (Mn^{2+}) ion in the host nanocrystals can be achieved since the initial Mn^{2+} concentration is relatively high in the MnSe clusters.

Another remarkable doping method using Successive ionic layer adsorption and reaction (SILAR) was reported by Cao et al. to introduce Mn ions into the CdS/ZnS (core/shell) nanocrystals with fairly high luminescence quantum yield (>50%).[21] In this layer-by-layer synthesis, the host nanocrystals were synthesized at high temperature (250°C), followed by a couple of shell coating (ZnS) in the elevated temperature (280°C). Mn ions were doped in the shell layers in the CdS/ZnS core/shell nanocrystals. This synthetic route, which separates the nucleation of the host nanocrystals from the doping, suppresses the nucleation of additional host nanocrystals during the doping process. Moreover, controlling the dopant location in the shell enhance the embedment

of the dopant ions in the host nanocrystals preventing expulsion of the dopant ions out of the host nanocrystals.

2.1.2 Electronic Structure of Mn-Doped II-VI Semiconductor Nanocrystals

Quantum dots (QDs) are referred to as semiconductor nanocrystals whose size is small enough to show quantum mechanical properties. For the semiconductor nanocrystals whose diameter is less than exciton Bohr radius (a_B^*), electronic structure can be described by a particle in a box model in which the energy levels are determined by its physical size. a_B^* is defined as

$$a_B^* = \frac{\varepsilon_r m_0}{\mu} a_B \qquad (1)$$

where a_B(=0.053 nm) is the Bohr radius, ε_r is the relative dielectric constant, m_0 is the free electron mass, and μ is the reduced mass. Once excitons are confined in the small nanocrystals, energy levels are quantized and dependent on size of the nanocrystals (so-called quantum confinement/size effect). The most significant feature of the QDs is that the electronic structure of the nanocrystals can be tuned depending on the size, shape, and composition of the QDs. For the II-VI QDs such as CdS, CdSe, ZnS , and ZnSe, borrowing the ideas from molecular orbital (MO) theory, occupied MOs arise from a linear combination of atomic orbitals of chalcogen anions while unoccupied MOs from metallic cations. In order to avoid confusion on the terms of the energy levels, the occupied MOs and unoccupied MOs in the QDs will be termed valence band and conduction band respectively in this dissertation, borrowing the language of the solid state physics. Energy difference between bottom edge of the conduction band and top

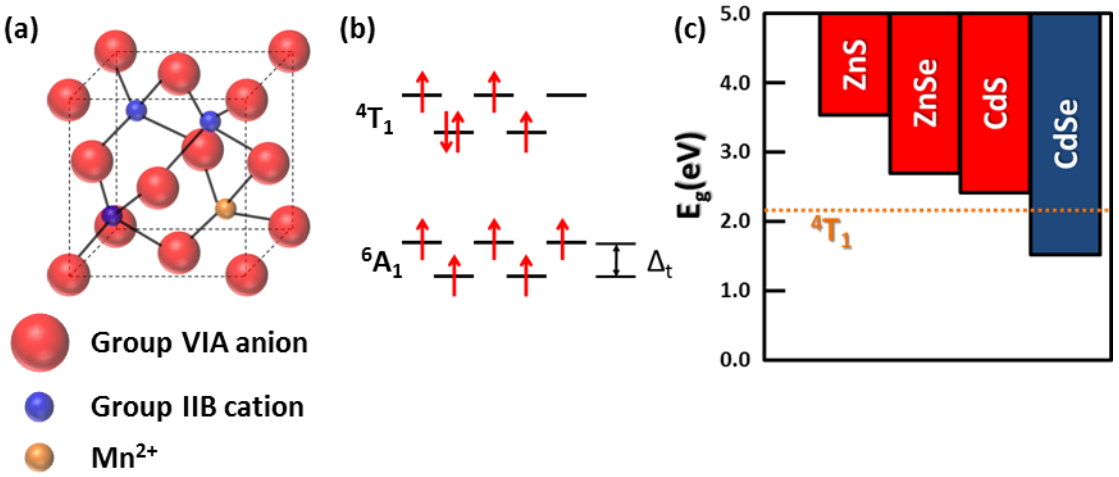

Figure II-1. (a) Zinc blende crystal structure of Mn-doped II-VI nanocrystals. (b) Electronic configuration of the lowest excited state ($^4T_1$) and ground state ($^6A_1$) of Mn2+ ions in tetrahedral sites. (c) Comparison between the lowest excited energy state of Mn^{2+} ions in the ligand field and bulk band gaps of typical II-VI semiconductor nanocrystals.

edge of the valence band is referred to as bandgap. Once the QDs are optically excited with sufficiently high photon energy, electron is excited from the valence band to the conduction band, generating electron-hole pair known as exciton. Afterwards, the electron and hole in the excited state rapidly relax to its bottom and top of the conduction and valence band respectively followed by excitonic interband transition, giving rise to excitonic luminescence (so-called band-gap emission).[7]

In Mn-doped II-VI QDs, the most common crystal structure is zinc blende in which cations at tetrahedral sites are substituted by Mn^{2+} ions, which are affected by the tetrahedral ligand field as shown in Figure II-1(a). Figure II-1(b) exhibits the ground state of Mn^{2+} ions (five 3d electrons) is symmetric ($^6A_1$) in the typical weak ligand field, and 5-fold degenerate 3d orbitals split into t_2 and e sets (Δ_t). In this ligand field, the lowest excited state is $^4T_1$ state. The offset of the host nanocrystals conduction band

relative to the lowest excited energy level of Mn^{2+} ions dictates many of the system's optical properties as shown in Figure II-1(c). The two most common cases are; 1) the bottom of the conduction band in the nanocrystals is higher than the energy level of the Mn^{2+} excited state, and 2) the bottom of the conduction band is lower than the Mn^{2+} excited state. The first case is commonly found when Mn^{2+} ions are doped into ZnS, ZnSe, or CdS. The excited states of the Mn^{2+} ions are isolated from the excitonic state. The Mn luminenescence in this case is originated from the ligand field d-d transition ($^4T_1 \rightarrow {}^6A_1$) of the Mn^{2+} ions, in which $^6A_1$ is ground state and $^4T_1$ the first excited state. The ligand-field transition is spin-forbidden to give rise to extremely small value of molar extinction coefficient ($10^0 - 10^1$ $M^{-1}cm^{-1}$ at its maximum) compared to the excitonic molar extinction coefficient ($10^5 - 10^6$ $M^{-1}cm^{-1}$ at its first excitonic absorption peak). The lifetime of the Mn luminescence is in the range of hundreds of microseconds up to a few milliseconds due to the nature of the spin forbidden ligand-field transition. The second case is commonly found when Mn^{2+} ions are doped into CdSe, the excited states of the Mn^{2+} ions are buried in the conduction band of the host nanocrystals. Although the luminescence from the Mn-doped CdSe QDs is the excitonic emission, the characteristics of the luminescence are strongly affected by the Mn ions via sp-d exchange coupling, which will not be discussed in detail in this dissertation.[23,70]

2.1.3 Dynamic Processes in Phtoexcited Mn-Doped II-VI Semiconductor Nanocrystals

Characterization of the dynamic processes can be accomplished by transient absorption measurement, which uses a pump pulse (generating excitons in the host

nanocrystals) and a probe pulse (measuring the population of the excited state exciton at different pump-probe delay time). Difference of optical density at specific wavelength is measured as a function of time with and without the pump excitation. Information about the dynamics of electro/hole can be obtained by selecting appropriate pump or probe wavelengths, which are described in detail in the recent studies by Chen et al..[25,49]

For photoexcited undoped QDs , the exciton relaxes via radiative and nonradiative electron/hole recombination. The radiative recombination process gives rise to exciton luminescence, and nonradiative recombination usually result in trapped charge carriers. The quantum efficiency of the exciton luminescence is dictated by relative efficiency of both the radiative and nonradiative pathways. Radiative relaxation of the exciton (several tens of nanoseconds) typically occurs slower than nonradiative recombination (sub-nanosecond), resulting in relatively low luminescence quantum yield. Moreover, delocalization of the exciton in the nanocrytals results in facile trapping of the exciton in defect sites.[71]

In photoexcited Mn-doped QDs, in which the excited state Mn^{2+} energy level lies within the bandgap, the exciton can transfer its energy to Mn^{2+} ions. The exciton to Mn^{2+} energy transfer occurs faster (within a few picoseconds) than either radiative and nonradiative relaxations (typically several tens of nanoseconds and sub-nanosecond respectively).[25] It means that the exciton-Mn energy transfer avoids the nonradiative relaxation pathways, resulting in increase of luminescence quantum efficiency. Once the ligand-field states of the Mn^{2+} ion are excited by the energy transfer, the Mn-doped QDs emit the sensitized Mn luminescence, which is highly efficient because the localized

energy states of Mn^{2+} ions are barely affected by nonradiative relaxation. Compared to the rate of the dynamic processes of the exciton, the lifetime of the sensitized Mn luminescence is extremely slow due to the nature of the spin-forbidden transition (several hundreds of microseconds to a few milliseconds). The long-lived excited states of the Mn ions can function as energy reservoir which can be utilized for light harvesting even though it is not beneficial for light-emitting application purposes.

2.1.4 Optical Properties in Mn-Doped II-VI Semiconductor Nanocrystals

Optical properties of the Mn luminescence in the Mn-doped QDs can be characterized as extinction coefficient, spectrum, luminescence lifetime, and luminescence quantum efficiency. Since the molar extinction coefficient of Mn^{2+} ion ($10^0 - 10^1$ $M^{-1}cm^{-1}$ at its maximum) is significantly smaller than the typical semiconductor nanocrystals ($10^5 - 10^6$ $M^{-1}cm^{-1}$ at its first excitonic absorption peak), it is extremely difficult to excite the ground state Mn^{2+} ion directly. However, the excitation of Mn^{2+} ion can be accomplished with significantly high efficiency of the energy transfer from the exciton (nearly 90% in the most efficient system). The rapid energy transfer helps to suppress electron and hole trapping of the exciton, which is the most common cause of luminescence quenching. Therefore, the excitonic energy efficiently transferred to the Mn^{2+} ion is emitted as a photon through the ligand-field transition with high quantum efficiency due to the localized nature of the ligand-field transition. For example, the quantum yield of Mn luminescence in Mn-doped CdS/ZnS core/shell QDs is nearly 80% ,which is larger than the exciton luminescence quantum

yield from undoped CdS/ZnS QDs (~35%). This disparity in the quantum yield is explain by the dopant mediated suppression of the nonradiative relaxation.[50] Furthermore, the quantum yield of the Mn luminescence can be enhanced by surface modification such as addition of thiols on the surface of nanocrystals, recovering trapped-excitons to dopant via ligand-assisted energy transfer .[72]

The transition energy of the Mn luminescence depends on both the pairing energy and ligand-field splitting.[73,74] In this study, the typical peak wavelength and bandwidth of the ligand-field Mn luminescence at room temperature are ~610 nm and ~70 nm respectively, which is largely red-shifted and broadened from the band-edge excitonic emission (~440 nm and ~25 nm). The peak wavelength of the Mn luminescence is strongly affected by doping concentration and chalcogenide ligand at a given temperature. The Mn luminescence can be tuned by local lattice strain on the Mn^{2+} ions. This can be accomplished via manipulation of core sizes, shell thicknesses, and the composition of the core/shell nanocrystals.[75,76] Larger local lattice strain on the dopant sites increases the ligand field splitting, which results in decrease of the transition energy and red-shift of the Mn luminescence. Furthermore, the local lattice strain on the dopant sites can manipulate the frequency of local vibrational modes and the local thermal expansion property of the dopant sites, which is temperature dependent. For example, as local lattice strain loaded on the dopant sites increases, the vibrational frequency coupled to Mn luminescence decreases, exhibiting more significant broadening in the luminescence bandwidth with temperature increase. In addition, increase of the local lattice strain at the dopant sites gives rise to the enhanced local thermal expansion at the

dopant sites, which results in more dramatic shift of the peak wavelength within given temperature changes.

2. 2 Plasmon-Controlled Luminescence

2.2.1 Optical Properties of the Plasmonic Metal Nanoparticles

A plasmon is known as a collective oscillation of conduction electrons in a noble metal or a heavily doped semiconductor. [27] When the plasmon is confined in the small nanoparticles relative to the wavelength of the incident light, it is called a localized surface plasmon (LSP). A large optical extinction coefficient ($\sim 10^6 - 10^9$ $M^{-1}cm^{-1}$ at its maximum of plasmon resonance wavelength) and enhanced electric field near the particle's surface are essential features of the plasmonic metal nanoparticles (MNPs) due to the LSP. The extinction cross section of an optical species determines probability of interaction between the incident light and the optical species, e.g. scattering and absorption of light depend on the extinction cross section of the MNP, and increase/decrease with the magnitude of the cross section. Compared with other optical species such as organic molecules and semiconductor nanoparticles, the extinction cross section of the plasmonic MNPs is significantly larger, even after accounting for the physical sizes of the optical species, Figure II-2(a). If the ratio between the extinction cross section and physical cross section is considered as a comparison of the photon and optical species interaction strength, the plasmonic MNPs show the strongest interaction, where this ratio is larger than unity only in the plasmonic MNPs, Figure II-2(b).

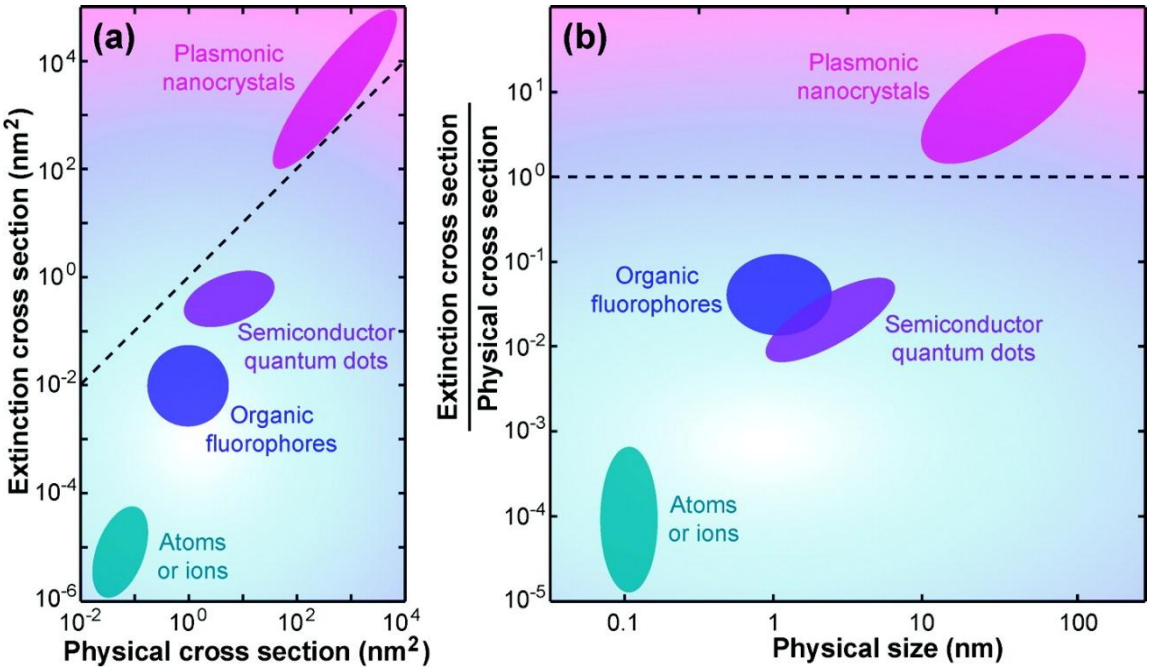

Figure II-2. (a) Extinction and physical cross sections of different kinds of optical species. (b) Ratio between the extinction and physical cross sections versus physical sizes of the optical species. Figure adapted from Ming's work.[29]

The electric field (**E**) near a spherical MNP can be determined by solving LaPlace's equation ($\nabla^2\Phi$), where the nanoparticle of radius R and complex dielectric constant (ε_s), is assumed to exist in isotropic, non-absorbing, medium with dielectric constant (ε_m). If a uniform electric field is applied to the system, the field in the particle is found by solving ($\mathbf{E} = -\nabla\Phi$), the solution to the Laplace's equation in spherical coordinates is of interest

$$\frac{1}{r^2 sin\theta}\left[sin\theta\frac{\partial}{\partial r}\left(r^2\frac{\partial}{\partial r}\right)+\frac{\partial}{\partial\theta}\left(sin\theta\frac{\partial}{\partial\theta}\right)+\frac{1}{sin\theta}\frac{\partial^2}{\partial\phi^2}\right]\Phi(r,\theta,\phi)=0 \qquad (2)$$

The solution to the LaPlace's equation is a combination of angular solutions (in the form of spherical harmonics) and radial solutions (in the form of r^l *and* $r^{-(l+1)}$ where *l* is the angular momentum number of atomic orbitals). A general solution to the

equation has the form below due to the azimuthal symmetry, independent of ϕ, where $\Phi_{In}(r,\theta)$ and $\Phi_{Out}(r,\theta)$ are the electric potential inside and outside the spherical MNP respectively.

$$\Phi_{In}(r,\theta) = \sum_{l=0}^{\infty} A_l r^l P_l(cos\theta) \tag{3}$$

$$\Phi_{Out}(r,\theta) = \sum_{l=0}^{\infty} (B_l r^l + C_l r^{-l-1}) P_l(cos\theta) \tag{4}$$

where two boundary conditions for the equation should be met; 1) the electric potential and 2) displacement field ($\mathbf{D} = \varepsilon\mathbf{E}$) is continuous at the surface of the spherical MNP.

Once the two boundary conditions are applied to the equations, the solutions for the equation (l=1) are evaluated as below

$$\Phi_{In}(r,\theta) = -\frac{3\epsilon_m}{\epsilon_s + 2\epsilon_m}\mathbf{E_0} r cos\theta \tag{5}$$

$$\Phi_{Out}(r,\theta) = -\mathbf{E_0} r cos\theta + \frac{\epsilon_s - \epsilon_m}{\epsilon_s + 2\epsilon_m}\mathbf{E_0}\frac{R^3}{r^2} cos\theta \tag{6}$$

Here the electric field outside the nanoparticle ($\mathbf{E_{Out}}$) is of interest, which can be expressed as

$$\mathbf{E_{Out}} = \mathbf{E_0} + \frac{1}{4\pi\epsilon_0\epsilon_m}\frac{3\mathbf{n}(\mathbf{n}\cdot\mathbf{p}) - \mathbf{p}}{r^3} \tag{7}$$

where the first term represents the applied field ($\mathbf{E_0}$) of the incident light and the second the induced dipole field. Here $\mathbf{n} = \mathbf{r}/r$ is the unit vector along the direction of the incident light (external field), and $\mathbf{p}$ is the induced dipole moment of the plasmonic MNP by the external field.

$$\mathbf{p} = 4\pi\epsilon_0\epsilon_m a^3 \frac{\epsilon_s - \epsilon_m}{\epsilon_s + 2\epsilon_m}\mathbf{E_0} = 4\pi\epsilon_0\epsilon_m\alpha\mathbf{E_0} \quad (8)$$

with the polarizability (α) defined as

$$\alpha = R^3 \frac{\epsilon_s - \epsilon_m}{\epsilon_s + 2\epsilon_m} \quad (9)$$

Therefore, the electric field near the spherical MNP is affected by a combination of MNP size, dielectric constants of the MNP/medium, and the external field.

2.2.2 Plasmon-Modified Luminescence of Typical Luminophores

Photoluminescence (PL) intensity (*I*, photon counts collected at emission wavelength per unit time) of a luminophore can be described by

$$I = \Gamma_E \times \Phi_{PL} \times \Phi_{Col} \quad (10)$$

where Γ_E is the excitation rate (absorbed photon counts to excite the luminophore at excitation wavelength per unit time), Φ_{PL} is quantum efficiency of the PL, and Φ_{Col} is the light collection efficiency which is dependent on the optical measurement system. The excitation rate can be described by Fermi's golden rule below

$$\Gamma_E = \frac{4\pi^2}{h}\langle f|\mathbf{E}\cdot\mathbf{P_T}|i\rangle^2\rho_e \quad (11)$$

where *h* is Planck's constant, *i* and *f* are wave function of the initial and the final state, and ρ_e is the density of the excited state. The perturbation operator consists of a local

electric field (**E**) and a transition dipole moment ($\mathbf{P_T}$) of the luminophore. The PL quantum efficiency of a typical luminophore is determined by the ratio of the rate constant for radiative pathway and the sum of all the decay pathways in the luminophore as

$$\Phi_{PL} = \frac{k_r}{(k_r + k_{nr})} \tag{12}$$

In the vicinity of a plasmonic MNP, the local electric field near the luminophore can be enhanced by the induced dipole field of the plasmon resonance. This occurs because of the large local electric field enhancement in near the surface of the metal due to the plasmon interaction with light. Therefore, the plasmon enhanced luminescence intensity of a luminophore can be expressed as

$$I' = \Gamma'_E \times \Phi'_{PL} \times \Phi_{Col} \tag{13}$$

where Γ'_E and Φ'_{PL} are the plasmon-modified excitation rate and PL quantum efficiency respectively, where the luminophore is in vicinity of the plasmonic MNP.

Here the modified quantum efficiency of the luminescence can be described with an extra relaxation channel of the energy transfer from the excited luminophore to the plasmonic MNP.

$$\Phi'_{PL} = \frac{k_r}{(k_r + k_{nr} + k'_{ET})} \tag{14}$$

where k'_{ET} is a rate constant of energy transfer from the excited luminophore to the adjacent MNP while assuming the plasmonic MNP does not affect other rate constants of the relaxation pathways.

The ratio between those two luminescence intensities can be written

$$\frac{I'}{I} = \frac{\Gamma'_E \times \Phi'_{PL} \times \Phi_{Col}}{\Gamma_E \times \Phi_{PL} \times \Phi_{Col}}$$

$$= \frac{\Gamma'_E}{\Gamma_E} \times \left(\frac{k_r}{(k_r + k_{nr} + k'_{ET})}\right) \Big/ \left(\frac{k_r}{(k_r + k_{nr})}\right)$$

$$= \frac{\Gamma'_E}{\Gamma_E} \times \frac{k_r + k_{nr}}{k_r + k_{nr} + k'_{ET}} = P_E \times P_Q \quad (15)$$

where P_E and P_Q are the excitation enhancement factor and quenching factor for the luminescence respectively. Those two factors show distance (d) dependence between the centers of the luminophore and MNP as below

$$P_E(d) = \left(\frac{R_E}{d}\right)^{n_E} + 1 \quad (16)$$

where R_E is the constant for the distance at which twice the luminescence enhancement is observed, and n_E is the constant depending on the distance and orientation of the interacting dipoles .[77]

$$P_Q(d) = \frac{1}{\left(1 + \left(R_Q/d\right)^{n_Q}\right)} \quad (17)$$

where R_Q is the constant for the distance at which $k'_{ET} = k_r + k_{nr}$, and n_Q is the constant varying between 3 and 6 depending on the geometric arrangement of the interacting dioples.[78-80]

2.2.3 Plasmon-Modified Luminescence of Mn-Doped Semiconductor Nanocrystals

In Mn-doped QDs, I'_{Mn}/I_{Mn} is determined by adjusting the exciton–Mn energy transfer quantum yield ($QY_{ET} = k_{ET}/(k_{r,ex} + k_{nr,ex} + k_{Q,ex}(d) + k_{ET})$) for the presence of the plasmonic MNP

$$\frac{I'_{Mn}}{I_{Mn}} = P_E(d) \times \frac{k_{r,Mn} + k_{nr,Mn}}{k_{r,Mn} + k_{nr,Mn} + k_{Q,Mn}(d)} \times \frac{k_{ET}}{k_{r,ex} + k_{nr,ex} + k_{Q,ex}(d) + k_{ET}} \quad (18)$$

where the rate constants are described as below

$k_{r,ex}$, $k_{r,Mn}$: radiative rate constants for exciton and Mn luminescence

$k_{nr,ex}$, $k_{nr,Mn}$: nonradiative rate constants for exciton and Mn luminescence

k_{ET} : energy transfer rate between exciton and Mn

$k_{Q,ex}$, $k_{Q,Mn}$: quenching rate constant for exciton and Mn luminescence by the MNP

Based on the typical reported values,[49,50] for Mn-doped QDs $k_{ET} \gg k_{r,ex} + k_{nr,ex}$, and the QY_{ET} can be approximated as $k_{ET}/(k_{Q,ex}(d) + k_{ET}) = 1/(1 + (R_{ET}/d)^n)$ in which R_{ET} is the distance constant at which $k_{Q,ex}(d) = k_{ET}$. Therefore, I'_{Mn}/I_{Mn} can be expressed as

$$\frac{I'_{Mn}}{I_{Mn}} \approx P_E(d) \times \left(\frac{1}{1 + \left(\frac{R_{Q,Mn}}{d}\right)^{n_{Q,Mn}}} \right) \times \left(\frac{1}{1 + (R_{ET}/d)^n} \right) \quad (19)$$

According to the equation above, for Mn-doped QDs adjacent to the plasmonic MNP, the plasmon-induced change of Mn luminescence intensity scales as a function of distance between the Mn-doped QDs and plasmonic MNP, being affected by two factors;

1) interaction strength between interacting dipoles of Mn luminescence and LSP, and 2) exciton-Mn energy transfer rate.

2.3 Luminescence Nanothermometry

2.3.1 Ratiometric Luminescence Nanothermometry

Recent progress in luminescence nanothermometry using temperature-dependent luminescence of various molecular and nanocrystalline materials has been accomplished due to the ability to optically measure the temperature with high accuracy (<0.1 ºC) and spatial resolution (<10 μm).[51-62] Luminescence nanothermometry has been applied to the temperature sensing of various platforms such as micro/nanofluidics, integrated devices and intracellular environment measurements.[81-86] The temperature dependence of various optical properties such as: intensity, spectral position, bandwidth, polarization and lifetime are among the frequently utilized temperature sensing mechanisms in luminescence thermometry.[53-56]

Among those luminescence nanothermometry methods, ratiometric measurement of multiple emitters has become more common recently, where the temperature-dependent ratio of the luminescence intensities from the two emitters is measured instead of the absolute intensity. For this type of measurement to be made, dual emitting materials must be used such as 1) rare earth ion-doped nanoparticles or metal-organic framework (two dopant emissions), 2) Mn-doped quantum dot (exciton and dopant emissions), and 3) organic dye-doped semiconducting polymer dots.[57-62] Since the intensity ratio fluctuates much less than the absolute intensity, which varies depending

on emitters' concentration, excitation intensity variation, and different emission collection efficiency between different measurement systems, the ratiometric thermometry is generally more accurate than non-ratiometric methods for the optical temperature imaging.

For the rare earth ion-doped nanoparticles, Brites et al. introduced synthesis of Eu^{3+}, Tb^{3+} co-doped γ-Fe_2O_3 nanoparticles as a dual emitter for luminescent nanothermometer. In this system, the temperature dependent luminescence originates from the $^5D_4$ (Tb^{3+}) emission line, while emission from the $^5D_0$ excited state of the Eu^{3+} remains nearly temperature independent, functioning as an internal reference. The excited energy state of the host, which is slightly above the $^5D_4$ in Tb^{3+} energy level, gives rise to energy transfer between the dopant and host states. This energy transfer shows strong temperature dependence as it is a phonon-assisted process.[58]

Consequently, Vlaskin et al. reported the tunable dual emission from Mn-doped quantum dot which shows strong temperature dependent luminescence originating from two emissive excited states from the exciton and dopant. PL from the $Zn_{1-x}Mn_xSe$/ZnCdSe core/shell nanocrystals show the characteristic Mn^{2+} ligand-field transition ($^4T_1 \rightarrow {}^6A_1$) around 600 nm, and the excitonic PL around 440 nm. The ratio between the dopant and excitonic PL intensities varies as a function of temperature. As temperature increases, the population of the Mn^{2+} excited state decreases due to thermal de-trapping back to the excitonic state. Therefore, the PL spectrum is dominated by the dopant luminescence at low measurement temperature (223K) and the excitonic luminescence at high temperature (403K). Furthermore, the active temperature window

of the measurement can be scaled adjusting the size of core diameter.[60]

Recently, the synthesis of Rhodamine B (RhB)-doped semiconducting polymer dots (Pdots) was reported by Ye et al. for the ratiometric temperature sensing. The temperature sensitive luminescence from the RhB was measured, and the nearly constant luminescence from the Pdots was used as an internal reference. As observed in other ratiometric nanothermometry, the ratio between the two luminescence intensities was used as indicator of the temperature variation. Even though the RhB-doped Pdots showed a narrow temperature window, they exhibited several intriguing features such as fairly large luminescence quantum efficiency (30%), non-toxic organic based compositions, and the temperature range of the measurement was (10−70 ºC) which is good enough for use in physiological system.[62]

While those ratiometric nanothermometry methods allowed for more robust intensity-based luminescence nanothermometry, minimizing the impact from other environmental conditions remains a challenge. For instance, luminescence intensity and peak position of many thermo-sensitive dye molecules vary significantly as the polarity or pH of the surrounding medium changes.[63,64] In the case of quantum dots, the variation of the surface functionalization and interparticle distance can change the exciton luminescence intensity and spectrum.[87-89] For instance, the luminescence intensities of the exciton and dopant emission in nanocrystals are affected differently when charge carrier-accepting molecules (e.g., thiols) are attached to the surface, or if dissolved oxygen is present in the surrounding medium.[90,91] Therefore, an optical species, which emits chemically insensitive and strongly temperature-dependent luminescence is ideal

for ratiometric luminescence nanothermometry.

2.3.2 Tuning Temperature-Dependent Mn Luminescence

One strategy which has been effective in reducing the environmental sensitivity of quantum dot luminescence has been to coat the emitting quantum dot with a 'shell' material, forming a barrier between the emittor and the surrounding medium. For example, CdS quantum dots are commonly coated with an intert ZnS shell, effectivly isolating them from the surrounding medium. For Mn-doped CdS/ZnS core/shell QDs, in which the Mn is doped in the ZnS layer, the Mn luminescence spectral lineshape is highly robust with respect to the change in the surrounding medium such as, polarity, phase, and pH, and is even insensitive to nanocrystal aggregation, since the Mn^{2+} dopant ions are embedded far below the surface of the nanocrystals (a few layers of the shell) with controlled doping radius.

Recently Chen et al. reported temperature dependence of the Mn luminescence spectrum in Mn-doped CdS/ZnS QDs by adjusting local lattice strain at the Mn^{2+} site through control over the radial doping location and doping concentration. Tuning the local lattice strain affects the frequency of the local vibrational modes and local thermal expansion properties of the Mn luminescence spectrum, whose peak position and bandwidth are changed with different degrees of the temperature dependence via the modification.

In the study, the local lattice strain at the Mn^{2+} dopant site was controlled by varying the radial doping location (d) of the Mn^{2+} ions for a given CdS/ZnS QD as

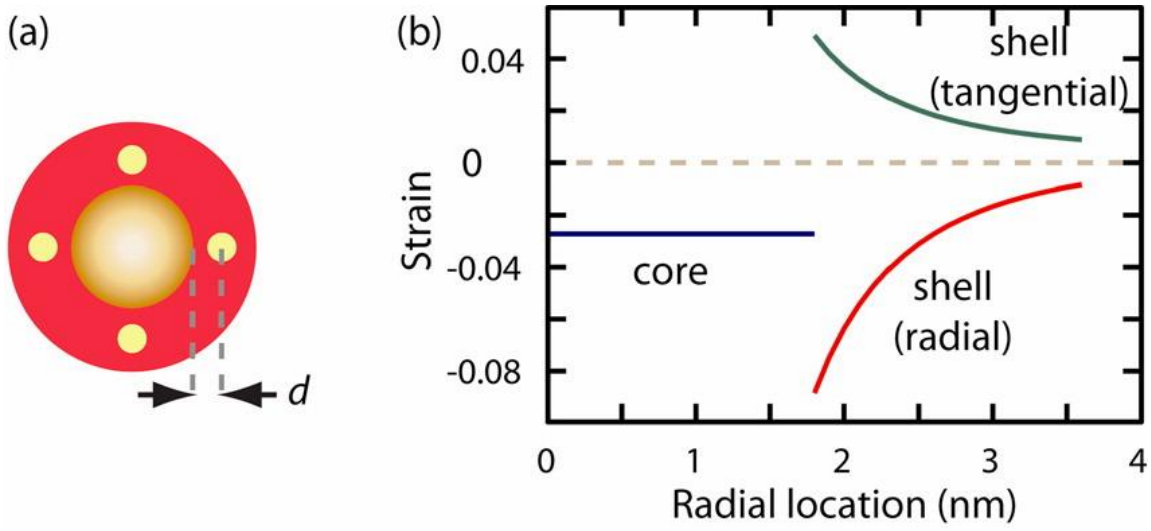

Figure II-3. (a) A schematic of Mn-doped CdS/ZnS core/shell QDs with radial doping location (d) of Mn^{2+} ion (yellow small dot). (b) Calculated strain of CdS/ZnS core/shell QDs with size of core radius (1.8nm) and shell thickness (1.8nm). Figure adapted from Chen's work.[26]

shown in Figure II-3(a). The lattice strain at a given location in the host structure was obtained by calculating a simple continuum model with an assumption of continuous interface between spherical core and zinc blende shell.[92,93] Figure II-3(b) shows the calculated strains in the core and shell (radial/tangential) where the diameter of core and thickness of shell are 3.6 and 1.8 nm respectively. Since lattice parameter of CdS (5.82 Å) larger than ZnS (5.41 Å) in bulk phase introduces lattice mismatch at the interface, the CdS core contracts in both tangential/radial directions while ZnS shell stretches in tangential direction to preserve the continuous interface and shrinks in radial direction. The loaded strain is maximized at the interface and gradually diminishes further from the interface. Based on the calculated strain, the substituted Mn^{2+} ions are assumed to experience the local lattice strain at a given distance from the interface. Control over the local lattice strain gives rise to an adjustment of the ligand-field and bond strength

between the ZnS matrix and the Mn^{2+} ions, which affects the electronic/vibrational energy levels of the Mn^{2+}. Since Mn luminescence is a ligand-field transition, as described earlier, its luminescence spectrum is influenced the local ligand field which is strongly influenced by the local lattice strain. Therefore, modification of the local lattice strain, should modify the electronic and vibrational energy levels, resulting in changes to the temperature dependent luminescence spectrum.

Two distinguished features in the temperature-dependent Mn luminescence, which are attributed to tuning of the local lattice strain, are bandwidth change and peak position (E_{Max}) shift. The frequency (ω) of the vibrational mode coupled to the Mn^{2+} ligand-field transition is a key parameter which determines the temperature dependence of the emission line shape. Based on the analysis, ω becomes smaller (softens) as the local lattice strain increases, leading to fast broadening of Mn luminescence bandwidth with temperature increase. Furthermore, ω softens more with increasing doping concentration for a given doping location, which is attributed to the mismatch between the lattice parameters of MnS (5.22 Å) and ZnS (5.41 Å). E_{Max} of Mn luminescence shows a complicated temperature dependence compared to the bandwidth. E_{Max}increases (blue-shifts) with temperature increase in the range of 90-320 K due to two main contributions; 1) thermal expansion of the lattice decreases ligand-field splitting (10 Dq) of Mn^{2+} ions, which results in increase of the ligand-field transition energy ($^4T_1 \rightarrow {}^6A_1$).[94] 2) Higher vibrational frequency in $^4T_1$ with d5 high-spin electronic configuration gives rise to the blue-shift with temperature increase, which is considered less dominant factor. [95,96]

Therefore, understanding the effect of local lattice strain on the temperature dependence of Mn luminescence gives rise to utilization of the temperature dependent Mn luminescence for a nanothermometer application. Furthermore, synthetic control over Mn doping concentration and location in Mn-doped CdS/ZnS QDs can also be utilized to maximize or optimize the temperature dependence of Mn luminescence for specific application areas.

CHAPTER III

SYNTHESIS OF MN-DOPED CDS/ZNS CORE/SHELL QUANTUM DODTS AND EXPERIMENTAL METHODS*

3.1 Synthesis of Mn-Doped and Undoped CdS/ZnS Core/Shell Quantum Dots

3.1.1 Synthesis of Undoped CdS/ZnS Core/Shell Quantum Dots

CdS core was synthesized by injecting 2.0 mL of octadecene (ODE) solution with sulfur (0.25 M) to a mixture of ODE (12.0 mL), CdO (125 mg) and oleic acid (2.02 g) at 250 °C, and growing at 240 °C. The reaction was processed under the nitrogen condition. Once the desired size was achieved, the reaction was quenched by lowering the temperature. The core NCs are precipitated by centrifugation (2.5k rpm, 10min) after adding acetone (10mL) the mixture. Once the centrifugation was done, supernatant was decanted and toluene (2mL) was added to dissolve the precipitant followed by adding methanol (5mL) to the NCs solution. The rinsing step with toluene/methanol was repeated twice to remove all the unnecessary elements. The rinsed CdS core was further coated with a ZnS shell via SILAR (Successive Ionic Layer Adsorption and

---

*Reprinted in part with permission from Park, Yerok; Pravitasari, Arika; Raymond, Jeffrey E.; Batteas, James D.; Son, Dong Hee. Suppression of Quenching in Plasmon-Enhanced Luminescence via Rapid Intraparticle Energy Transfer in Doped Quantum Dots. *ACS Nano* **2013,** 7 (12), 10544-10551. Copyright 2013 by the American Chemical Society.

Reprinted in part with permission from Park, Yerok; Koo, Chiwan; Chen, Hsiang-Yun.; Han, Arum; Son, Dong Hee. Ratiometric Temperature Imaging Using Environment-Insensitive Luminescence of Mn-Doped Core–Shell Nanocrystals. *Nanoscale* **2013,** 5, 4944-4950. Copyright 2013 by the Royal Society of Chemistry.

Reaction) procedure using ODE solutions of sulfur (0.25 M) and zinc stearate (0.25 M) as the precursors. ZnS shell coating was achieved by injecting zinc streate in toluene and sulfur in ODE alternately to the mixture of the CdS NCs, OAm, and ODE at 220 °C with addition rate of 2 mL/min. After coating ZnS shells to the desired thickness, the solution was cooled to RT and washed following the same procedure as the CdS core NCs.

3.1.2 Synthesis of Mn-Doped CdS/ZnS Core/Shell Quantum Dots and Water-Soluble Ligand Exchange

Mn-doped CdS/ZnS core/shell (NCs) were synthesized following the procedures published elsewhere.[1-3] The key control in the synthesis of Mn-doped CdS/ZnS NCs was to dope Mn^{2+} at the desired location and doping concentration with the modified SILAR (Successive Ionic Layer Adsorption And Reaction) method. There were two types of doping routes in this study; 1) Mn^{2+} ion was embedded in the ZnS shell. 2) Mn^{2+} ion was inserted at the interface between the core and shell.

In order to dope Mn^{2+} in the ZnS shell, desired layers of the ZnS shell were firstly coated with the same procedure as the described above. Manganese (II) acetate was initially prepared in a degassed three-neck flask followed by adding oleylamine (OAm) under vacuum to prepare Mn precursor (0.02M), where the mixture was heated at 100 °C for 10 min. After then, the Mn precursor solution was added to the CdS/ZnS NCs dissolved in ODE and OAm at 260 °C for 20min. After doping Mn^{2+} process, the NCs were cooled to RT and washed by adding acetone and centrifugation. After the centrifugation, the precipitant was rinsed with methanol one time as same as the core

NCs. Finally, the desired layers of the ZnS shell were coated again with the same coating method.

To dope Mn^{2+} at the interface between the CdS core and the ZnS shell, manganese diethyldithiocarbamate was firstly prepared adding sodium diethyldithiocarbamate trihydrate in oleylamine (OAm) (0.015 M) to manganese (II) acetate in OAm (0.02 M) under nitrogen condition at 60°C. The prepared manganese diethyldithiocarbamate in OAm was added to the CdS core at 220 °C, which was prepared as same as the undoped QDs, The Mn-doped CdS NCs were precipitated with acetone, and then rinsed with toluene and methanol. ZnS shell coating was achieved by injecting zinc streate in toluene and sulfur in ODE alternately to the mixture of Mn-doped CdS NCs, OAm, and ODE at 220 °C. After coating ZnS shells to the desired thickness, the solution was cooled to RT and washed following the same procedure as the CdS core NCs. In the second study, Mn^{2+} ions were doped at the interface of the CdS core (1.8 nm in radius) and ZnS shell (1.8 nm in thickness). Since the cation and anion layers are added sequentially, the step at which the Mn precursor is introduced determines the radial location of the dopant.

In order to make the water-soluble QDs required for the deposition of the QD layer from the aqueous solution, ligand exchange was performed to replace the original surfactant with mercaptoundecanoic acid (MUA). The solution, which contains MUA in methanol/acetone 2:1 (v/v), was prepared to achieve pH of 10 by adding tetramethylammonium hydroxide. The ligand solution was added to the QDs solution to achieve the ligand exchange. The resulting MUA-passivated QDs were precipitated and

rinsed with a 1:1 mixture of ethyl acetate and petroleum ether before finally redispersed in Millipore water.

3.2 Determination of the Doping Concentration

ICP-MS and TEM were utilized to determine the concentration of Mn^{2+} ions per a CdS/ZnS nanocrystal where the diameter of the CdS core was verified as 3.6 nm by TEM. For the ICP-MS analysis, two sets of standard solutions were initially prepared to obtain calibration curves for Cd^{2+}/Zn^{2+} ions and Mn^{2+} ions. A series of concentration of the two different standard solutions were prepared by diluting 1ppm standard solution commercially available from Aldrich; 1) 2, 20, 50, and 100 ppb for Mn ion. 2) 20, 50, 100, 200, and 400 ppb for Cd^{2+}/Zn^{2+} ions. 1% nitric acid in Millipore water was used for the dilution. 1 mL of Mn-doped CdS/ZnS nanocrystals in hexane (OD ≈ 0.1 at 430 nm) was dried under nitrogen gas flow. After complete evaporation of the solvent, the nanocrystals were digested by adding highly pure nitric acid for quantitative trace metal analysis (BDH) and put under sonication for 10 min. About half of the solution after centrifugation was taken for further dilution, carefully not taking organics in the solution. For the two different test samples (Mn^{2+} and Cd^{2+}/Zn^{2+} ions), there were two types of dilution factors used to fit to the right range in the calibration curve. Initially the digested solution was diluted about 20 times for Mn^{2+} ion sample solution, and further diluted up to 300 times for the Cd^{2+}/Zn^{2+} sample solution. During all the steps of the preparation, mass (4 decimal digits of precision) and density of the solution were used to obtain the dilution factors. Once the molar concentration of the ions was determined by the

elemental analysis, the number of Mn^{2+} ions per a nanocrystal $\langle n_{Mn} \rangle$ was obtained to divide the molar concentration $[Mn^{2+}]$ of Mn ions by the molar concentration [NC] of nanocrystals. [NC] was obtained by dividing molar concentration $[Cd^{2+}]$ of Cd^{2+} ions by average number (491) of Cd^{2+} ions per a CdS core (3.6 nm in diameter) where the size of the core was determined by TEM measurement.

$$\langle n_{Mn} \rangle = [Mn^{2+}]/[NC] \quad (20)$$

3.3 Measurement of Time-Dependent Mn and Exciton Luminescence Intensity

The time-resolved luminescence was measured using two different methods. For the Mn luminescence, a pulsed nitrogen laser (Stanford Research Systems, NL100, 3.5 ns pulse width) centered at 337 nm and photomultiplier tube (Hamamatsu, 982R) were used in conjunction with a digital oscilloscope (LeCroy, WaveAce). A 500 nm longpass filter was used to prevent the excitation light reaching the detector. For the exciton luminescence, a time-correlated single photon counting (TCSPC) technique was used to measure the time-resolved luminescence. A pulsed diode laser (Picoquant, 80 ps pulse width) centered at 405 nm operating at 10 MHz was used as the excitation source. The exciton luminescence filtered with 450 nm bandpass filter (fwhm = 50 nm) was detected with a TCSPC-enabled PMT, with channel binning of 32 ps over the full time window (100 ns) of the measurement. The time-resolved exciton luminescence was obtained at several different areas on the substrate on a confocal microscope (Olympus, FV-1000) using a fluorescence life time imaging (FLIM) technique. The average lifetimes (τ_{avg})

reported in Table IV-1 are $\tau_{avg} = \sum(a_i \cdot \tau_i^2)/\sum(a_i \cdot \tau_i)$, where a_i and τ_i are the amplitude and time constant obtained from the multi-exponential fit of the data.

3.4 Fabrication and Characterization of the Multilayered Structure on the Ag MNP-Patterned Substrate

Clean Si (111) substrates were prepared by immersing the wafer in piranha solution at 100 °C for 1 hr and rinsing with Millipore water. To make the stripe-patterned layer of (3-aminopropyl)triethoxysilane (APTES) used as the linker between the substrate and Ag MNPs, microcontact printing method was used.[97] The polydimethylsiloxane (PDMS) stamps used for this purpose were made using a Si template having 12 μm-wide stripe patterns with a pitch of 9 μm. The inking of PDMS stamp with APTES was done by dropping 1% aqueous solution of APTES on top of the stamp. After removing the excess APTES solution with dry nitrogen from the PDMS stamp, a patterned APTES layer was transferred to the Si substrate by making a direct contact between the stamp and the substrate. The APTES-patterned Si substrate was dried for 1 hr and subsequently immersed in the aqueous solution of Ag MNPs (Sigma-Aldrich, 10 nm in diameter) for 45 min to allow the selective adsorption of Ag MNPs to the APTES-coated region. After rinsing the substrate with Millipore water, the resulting structure on the Si substrates were patterned stripes of Ag MNPs. A representative topographic image of the patterned Ag MNP layer on Si substrate obtained with an atomic force microscope (AFM, Agilent Technologies 5500) is shown in Figure IV-1(b). The polyelectrolyte spacer layer that separates the Ag MNP layer and QD layer was

formed on top of Ag MNP layer using a layer-by-layer deposition method.[46,77] Oppositely charged layers of poly(diallyldimethylammonium chloride) and poly(sodium 4-styrenesulfonate) were alternately deposited from 0.5 M NaCl solutions of the polyelectrolyte. The thickness of the spacer layer was changed by varying the total number of layers deposited. The thickness of the spacer layer was measured from the topographic AFM images of the covered vs. uncovered regions of the substrate obtained with a WITec Alpha 300 AFM. The roughness of the polyelectrolyte layer surface in AFM image is ~ ±1 nm, while the actual surface roughness could be larger due to the finite lateral dimension of the AFM tip. The QD layer was deposited on top of the outermost spacer layer by dipping the substrate in the aqueous solution of 1:1 mixture of Mn-doped and undoped QDs for ~1 min and rinsing the substrate thoroughly with Millipore water. All AFM images were acquired under ambient conditions in tapping mode using commercially available aluminum-coated silicon AFM tips from Nanoscience Instrument (Phoenix, AZ) with nominal tip radii of less than 10 nm and nominal spring constants of 48 N/m.

3.5 Imaging of Plasmon-Enhanced Luminescence Intensity on the Patterned Structure

The luminescence from the QD layer formed on Si substrate was imaged with a home-built microscope constructed with a 50X objective (Nikon, CFI L Plan EPI SLWD) and a tube lens (Nikon, f=200mm). A liquid nitrogen-cooled CCD (Princeton Instrument, PI-LCX) was used as the imaging device and a405 nm *cw* diode laser (Crystalaser) was used as the excitation source. The laser beam directly illuminated the entire imaging area

(0.5×0.5 mm^2) of the Si substrate. A longpass filter (410 nm) was used to block the excitation light reaching the CCD. Bandpass filters centered at 450 nm (fwhm = 60 nm) and 600 nm (fwhm = 10 nm) were used to record the images of exciton and Mn luminescence respectively.

3.6 Measurement of the Temperature-Dependent Mn Luminescence Spectra

Mn-doped CdS/ZnS NCs mixed with poly(methyl methacrylate) were spin-coated on the sapphire substrate. The temperature was controlled in an open-cycle cryostat (ST-100, Janis) using liquid nitrogen as the cryogen. The NCs on sapphire substrate were excited by a 403 nm *cw* diode laser at a low power (< 1 mW at 5 mm beam diameter). The luminescence spectra were measured with a fiber optic-coupled CCD spectrometer (QE65 Pro, Ocean Optics). A 450 nm long pass filter was used to block the scattered excitation light. The transmittance spectra of the two bandpass filters used for imaging (600 and 650 nm, 10 nm bandwidth) were used to obtain the temperature calibration curve from the measured Mn luminescence spectra.

3.7 Fabrication and Surface Temperature Imaging of Cryo-Cooling Device

A cryo-cooling device was constructed to provide a temperature gradient from 77-260 K over ~12 mm distance. Thin film of Mn-doped NCs was formed on a glass substrate from the solution of the NCs dispersed in chloroform via spin-coating. On top of the NCs-coated glass substrate, 15 μm-thick PDMS layer was spin-coated and cured. The black PDMS substrate having a channel for the liquid nitrogen ($3\times3\times10$ mm^3,

w×h×l) was replicated from a polymer master mold fabricated using a 3D printer (ULTRA, envision TEC). Before applying the uncured black PDMS to the master mold, two silicon tubes were connected at the inlet and outlet port of the liquid nitrogen channel. The black PDMS was cured in an oven at 80 ºC for 1 hour and permanently bonded to the NCs-coated glass substrate. The device was placed in the enclosure made of black acetal resin blocks. The front of the enclosure has a glass window for the illumination and imaging purpose. The enclosure has the inlet and outlet port for the dry nitrogen gas used for flushing the interior of the enclosure.

The surface temperature profile of the cryo-cooling devices was measured with the optical setup. Liquid nitrogen flowing through the channel cooled the region of the glass substrate in contact with liquid nitrogen to 77 K. The dry nitrogen flow through the enclosure prevents frosting on the surface of the glass substrate and maintains the temperature gradient between 77 K and ambient temperature on the glass substrate. The cryo-cooling device was illuminated with a 365 nm UV LED and a collimating lens. 475 nm short-pass filter (F1) was placed after the LED to remove the red tail of the spectrum. A dichroic mirror (DMLP505R, Thorlabs) was used to reflect the excitation light from the LED and collect the luminescence from the device. A combination of an achromatic doublet lens (L2, focal length = 200 mm) and a microscope tube lens (L3, focal length = 200 mm) was used to image the surface of the device on the CCD camera (Princeton Instrument, PI-LCX) at 1X magnification. Temperature image was generated by taking the ratio of the two intensity images at 600 and 650 nm and using the calibration curve shown in Figure 2(b). Each intensity image at 600 and 650 nm was separately recorded

with 20 sec integration time by placing a bandpass filter (F3) in front of the CCD. With this setup, each pixel of CCD images 20x20 μm^2 area.

CHAPTER IV

SUPPRESION OF QUENCHING IN PLASMON-ENHANCED LUMINESCENCE VIA RAPID INTRAPARTICLE ENERGY TRANSFER IN DOPED QUANTUM DOTS*

4.1 Introduction

Enhancement of excitation or emission rates by noble metal nanostructures adjacent to a luminophore has been widely utilized as a way to increase the intensity of photoluminescence (PL) or electroluminescence.[29,46,98-104] The enhancement of absorption or emission rate resulting in a stronger luminescence arises from the enhanced local electric field by the localized surface plasmon or the modification of photonic mode and local dielectric environment in the vicinity of the metal nanostructures.[27,29,37] Enhancement of excitation has been extensively studied particularly with colloidal metal nanoparticles (MNPs) that exhibit strong plasmon resonance, due to the relatively easy synthesis of MNPs with widely tunable resonances in visible and near IR spectral region.[38-40] While such MNPs can enhance the excitation of luminophores via enhanced local electric fields, at close distances they can also quench the luminescence through energy transfer from the excited luminophore to the

---

*Reprinted in part with permission from Park, Yerok; Pravitasari, Arika; Raymond, Jeffrey E.; Batteas, James D.; Son, Dong Hee. Suppression of Quenching in Plasmon-Enhanced Luminescence via Rapid Intraparticle Energy Transfer in Doped Quantum Dots. *ACS Nano* **2013,** 7 (12), 10544-10551. Copyright 2013 by the American Chemical Society.

MNPs.[41-44] Because of the relatively broad plasmon spectrum of MNPs compared to the Stokes-shifted luminescence of typical luminophores, simultaneous enhancement of the two opposing processes, *i.e.* excitation and quenching of emission, is unavoidable in most cases. For this reason, the difference in the MNP-luminophore distance dependence of the excitation enhancement and luminescence quenching has been exploited to optimize the net plasmonic enhancement of the luminescence.[44,46,47]

Here, we show that the MNP-induced quenching of the luminescence from semiconductor quantum dots (QDs) can be partially suppressed via fast intra-particle exciton-dopant energy transfer in doped QDs resulting in a stronger net plasmon-enhancement of the luminescence. This is shown in Mn-doped CdS/ZnS QDs that exhibit sensitized Mn luminescence via fast exciton-Mn energy transfer occurring on a few ps time scale.[49,50] The sensitized Mn luminescence is significantly more red-shifted from both the exciton absorption and plasmon resonance of the MNP than exciton luminescence. Therefore, the fast exciton-Mn energy transfer process that rapidly separates the absorber (exciton) and emitter (Mn) can reduce the spectral overlap between the emitter and plasmon resonance of MNPs.[23] One might anticipate that such reduction in emitter-MNP spectral overlap will suppress MNP-induced quenching of the luminescence leading to a stronger net plasmon-enhancement of the luminescence in doped QDs compared to undoped QDs. In order to verify the expected advantage from sensitized luminescence, here we made a systematic comparison of luminescence enhancement by Ag-MNPs for both Mn-doped and undoped CdS/ZnS QDs. To examine this the net plasmon-enhanced luminescence of doped and undoped QDs were measured

simultaneously as a function of the average distance between a mixed layer of the two types of QD's and Ag MNP layer formed on a Si substrate using a patterned array of the Ag MNPs we have described in previous studies of plasmon enhanced luminescence of QDs.[77] In this comparison, Mn luminescence in doped QDs exhibited a stronger net enhancement than exciton luminescence in undoped QDs at an optimum QD-MNP distance of *ca.* 10 nm. At very short QD-MNP distances (*ca.* 2 nm) however, Mn luminescence exhibited a stronger net quenching than exciton luminescence. These observations can be described qualitatively using a kinetic model, accounting for all of the competing processes including exciton-Mn energy transfer and MNP-induced quenching of both exciton and Mn luminescence. The present study suggests that the sensitized luminescence from a sufficiently fast donor-acceptor energy transfer can be superior to that from simple plasmon-enhancement of the luminescence alone.

4.2 Results and Discussion

To make a systematic comparison of the plasmon-enhancement of luminescence in Mn-doped and undoped QDs, under the same environment and with the same average QD-MNP distance, a multilayered structure schematically shown in Figure IV-1(a) was fabricated using layer-by-layer assembly. Layers of Ag MNPs and QDs separated by a series of polyelectrolyte spacer layers were deposited on a Si substrate employing a previously reported procedure .[46,77] The details of the fabrication and characterization of the structures used are described in the Methods section. Briefly, patterned stripes of a single layer of Ag MNP (~10 nm in diameter) was initially deposited on a Si substrate

using microcontact printed pattern of (3-aminopropyl)triethoxysilane (APTES) as the linker between Si substrate and Ag MNPs.[97] As demonstrated in our recent work this structure creates regions with and without plasmon-enhancement on the same substrate with minimal variation of the dielectric environment enabling a robust measurement of the luminescence enhancement.[77] Figure IV-1(b) shows the AFM image of the Ag MNP-patterned Si substrate. The distance between the QD and MNP layers was varied by changing the spacer layer thickness (*t*). 1:1 mixture of Mn-doped and undoped CdS/ZnS QDs of the same diameter and surface passivation was used to form the top QD layer.

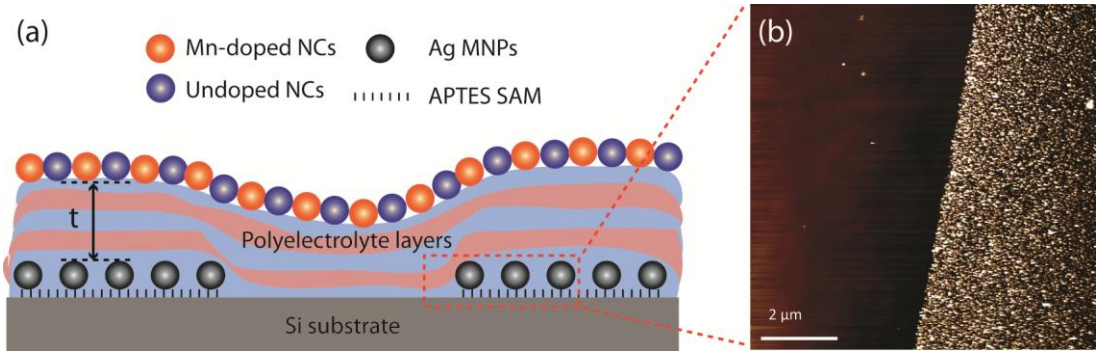

Figure IV–1. (a) Multilayer structure fabricated on Si substrate used for the comparison of plasmon-enhancement of exciton and Mn luminescence. (b) AFM image of the patterned Ag MNP layer on Si substrate before adding spacer and QD layer.

Figure IV-2 compares the absorption and luminescence spectra of Mn-doped and undoped CdS/ZnS QDs and the extinction spectrum of the Ag MNPs. Both Mn-doped and undoped QDs exhibit nearly identical absorption spectra consistent with having the same particle size observed in TEM (Supporting Information). The absorption coefficients of the doped and undoped QDs near the band-edge exciton absorption are

also nearly identical based on elemental analysis.[50] This ensures that both the doped and undoped QDs behave identically in the photoexcitation process. The plasmon resonance of the Ag MNPs near 400 nm overlaps well with the band-edge exciton absorption of the QDs centered at 420 nm. Exciton luminescence from the undoped QDs is centered at 440 nm close to the exciton band-edge absorption peak, while Mn luminescence from Mn-doped QDs is significantly more red-shifted occurring at ~ 600 nm. Due to the very efficient exciton-Mn energy transfer occurring on a few ps time scale, Mn-doped QDs used in this study exhibit only Mn luminescence without exciton luminescence. The spectral overlap integral J, defined as $\int F_d(\lambda)E_a(\lambda)\lambda^4 \, d\lambda$, where $F_d(\lambda)$ and $E_a(\lambda)$ are the normalized luminescence spectrum of donor and the molar extinction spectrum of Ag MNP respectively, was two orders of magnitude smaller for Mn luminescence compared to the exciton luminescence.

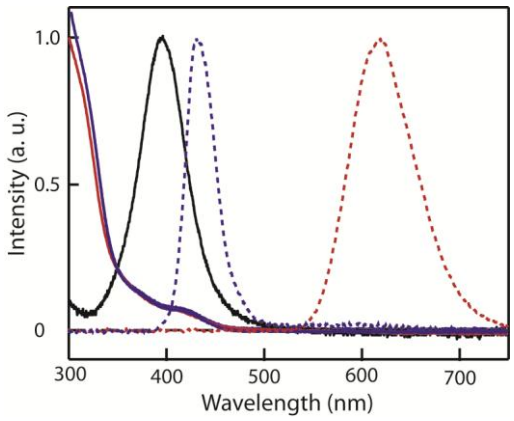

Figure IV–2. Comparison of the absorption (solid lines) and luminescence (dashed lines) spectra of the Mn-doped (red) and the undoped (blue) CdS/ZnS QDs. Extinction spectrum of the Ag MNPs is shown in black solid line. The QD luminescence and Ag MNP extinction spectra are normalized.

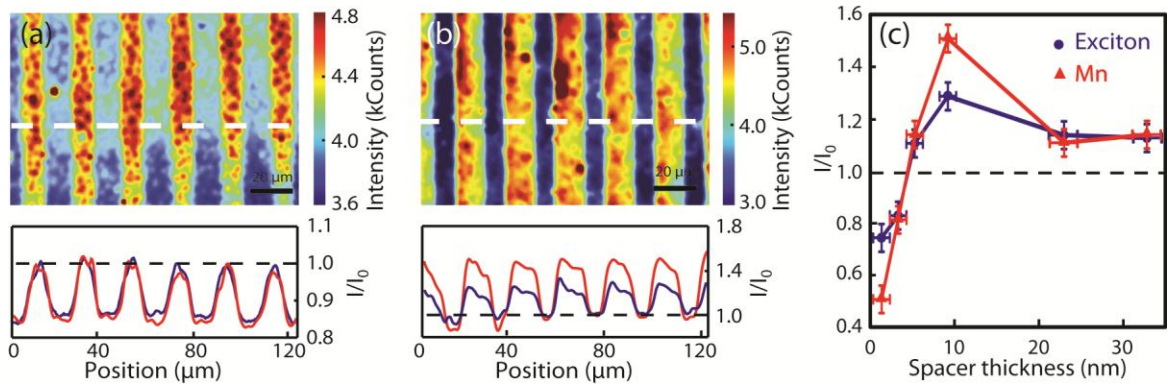

Figure IV–3. False-color images of Mn luminescence from the multilayered structure shown in Figure 1 with spacer layer thickness of 3 nm (a) and 9 nm (b). The bottom panels show the line profile of the intensity ratio (I/I_0) for Mn (red) and exciton (blue) luminescence at the region indicated with white dashed lines vertically averaged over 20 μm. (c) I/I_0 for exciton and Mn luminescence at different spacer layer thicknesses (t).

Figure IV-3(a) and (b) show the representative false-color images of the luminescence intensity from the fabricated multilayered structures under 405 nm excitation at two chosen spacer layer thicknesses (t), t = 3 nm and 9 nm for (a) and (b) respectively. The luminescence was imaged with a CCD camera and bandpass filters centered at 450 nm and 600 nm for exciton and Mn luminescence respectively. The line profiles of the intensity ratio (I/I_0) are also shown below each luminescence intensity image, where I and I_0 are the intensities from the regions with and without Ag MNPs respectively. Figure IV-3(c) compares I/I_0 with varying spacer layer thicknesses for both exciton (blue) and Mn luminescence (red). The maximum net enhancement occurs at a spacer layer thickness of t = 9 nm for both exciton and Mn luminescence. At this thickness, the Mn luminescence exhibits a stronger net enhancement than the exciton. With increasing thickness I/I_0 gradually decreases, while maintaining a net enhancement

of the luminescence. At shorter spacer layer thicknesses (*e.g.*, $t < 5$ nm), where the MNP-induced quenching of the luminescence outweighs the plasmon-enhanced excitation, the luminescence exhibits net quenching, *i.e.*, I/I_0 is < 1. Notably at the shortest spacer layer of $t < 2$ nm, the Mn luminescence exhibits a stronger net quenching than exciton luminescence in contrast to the stronger net enhancement observed at $t = 9$ nm. The comparison of the effect of Ag MNP/polyelectrolyte layer on the reflection and scattering efficiency of Si substrate at 450 and 600 nm indicates that the presence of the multilayer structure does not introduce any wavelength dependence of the overall luminescence photon collection efficiency. (See Supporting Information) Therefore, the difference in I/I_0 in Figure IV-3(c) reflects the actual differences in net plasmon enhancement of the two different emitters.

The important feature in Figure IV-3(c) is the stronger net enhancement (at $t = 9$ nm) and stronger net quenching (at $t < 2$ nm) of Mn luminescence compared to exciton luminescence, despite the same level of the excitation enhancement in both doped and undoped QDs. The observed difference in I/I_0 between doped and undoped QDs can be attributed to the following factors: (i) differences in the MNP-induced quenching of exciton and Mn, and (ii) competition between exciton-Mn energy transfer and other exciton relaxation channels. To obtain a better understanding of the different behaviors of I/I_0 observed for the doped and undoped QDs, we used a kinetic model shown in Figure 4(a) that includes all the major competing processes in the doped and undoped QDs adjacent to Ag MNP. In this model, $k_{r,i}$, $k_{nr,i}$, $k_{Q,i}$ ($i = ex, Mn$) represent the rate constants for the radiative relaxation, nonradiative relaxation in the absence of Ag MNP

and quenching by Ag MNP respectively for both exciton (i=ex) and the excited state of Mn (i=Mn). Here, k_{ET} represents the rate constant for exciton-Mn intra-particle energy transfer in Mn-doped QDs. In this model, we excluded the plasmon enhancement of the radiative decay rate of exciton in the consideration of the factors contributing to the enhancement of luminescence intensity. In principle, MNP plasmon can enhance both the excitation rate and the radiative decay rate with a varying degree depending on the details of the geometry of the plasmonic structure and the spectral overlap between the interacting transitions and excitation wavelength.[105,106] Under our experimental condition, where the spectral overlap is maximized among excitation wavelength, the plasmon of the isolated colloidal Ag MNP, and exciton absorption of QD, the enhancement of radiative decay of exciton is considered to be significantly less important than the excitation enhancement. This assumption is supported by the earlier studies that examined the enhancement of the local electric field and radiative decay rate of an emitter by the colloidal Ag MNPs, where the enhancement of radiative decay rate was significantly weaker than enhancement of local electric field at the relevant QD-MNP distances of this study.[107] While the model can be more refined with the inclusion of the enhancement of radiative decay rate, we used the simplified model excluding it since the essential features of the data shown in Figure IV-3(c) can be captured with less complexity of the model. In addition, in our study with randomly oriented dipoles of ensemble of QDs, the magnitude of plasmon enhancement is averaged over many different dipole orientations with respect to the electric field. Therefore, the dipole

considers only the average plasmon enhancement without explicit consideration on the dependence of the dipole orientation.

In the undoped QDs, the relative enhancement of exciton luminescence by the Ag MNP located at distance d from QD, $I_{ex}(d)/I_0$, is determined by the excitation enhancement factor ($P_{E,ex}$) and quenching factor ($P_{Q,ex}$) for the exciton luminescence as shown in Eq. 21. $P_{E,ex}$ represents the excitation enhancement by the plasmon-enhanced local electric field. The quenching factor for exciton, $P_{Q,ex}$, can be expressed as the ratio of the rate constants of all the competing processes,[108] where only $k_{Q,ex}$ depends on d. $P_{Q,ex}$ is often expressed as $1/(1+(R_{Q,ex}/d)^n)$, where $R_{Q,ex}$ is the distance at which $k_{Q,ex}(d)=k_{r,ex}+k_{nr,ex}$ and n varies between 3-6 depending on the geometric arrangements of interacting dipoles.[78-80,109]

$$I_{ex}(d)/I_0 = P_{E,ex}(d) \cdot P_{Q,ex}(d) = P_{E,ex}(d) \cdot \left(\frac{k_{r,ex} + k_{nr,ex}}{k_{r,ex} + k_{nr,ex} + k_{Q,ex}(d)} \right)$$

$$= P_{E,ex}(d) \cdot \left(\frac{1}{1 + \left(R_{Q,ex}/d\right)^n} \right) \quad (21)$$

$$I_{Mn}(d)/I_0 = P_{E,ex}(d) \cdot QY_{ET}(d) \cdot P_{Q,Mn}(d)$$

$$= P_{E,ex}(d) \cdot \left(\frac{k_{ET}}{k_{r,ex} + k_{nr,ex} + k_{Q,ex}(d) + k_{ET}} \right) \cdot \left(\frac{k_{r,Mn} + k_{nr,Mn}}{k_{r,Mn} + k_{nr,Mn} + k_{Q,Mn}(d)} \right)$$

$$\approx P_{E,ex}(d) \cdot \left(\frac{1}{1 + (R_{ET}/d)^n} \right) \cdot \left(\frac{1}{1 + \left(R_{Q,Mn}/d\right)^{n'}} \right) \quad (22)$$

In Mn-doped QDs, $I_{Mn}(d)/I_0$ is determined by the excitation enhancement factor for the exciton ($P_{E,ex}$), exciton-Mn energy transfer quantum yield (QY_{ET}) in the presence of a

Ag MNP and the quenching factor for Mn luminescence ($P_{Q,Mn}$) as described in Eq. 22. Both the doped and undoped QDs have the same $P_{E,ex}$, since their absorption spectra near the band-edge are identical. $P_{Q,Mn}$ is expressed as the ratio of the rate constants of the relevant competing processes or in terms of $R_{Q,Mn}$ defined similar to $R_{Q,ex}$. Here, $R_{Q,Mn}$ represents the average behavior of many Mn^{2+} ions doped in the QD. The energy transfer quantum yield (QY_{ET}) can also be expressed as the ratio of the rate constants. Since $k_{ET} \gg k_{r,ex} + k_{nr,ex}$ for Mn-doped QDs used in this study,[49,50] QY_{ET} can be approximated as $1/(1+(R_{ET}/d)^n)$, where R_{ET} is the distance at which $k_{Q,ex}(d)=k_{ET}$. For the Mn-doped QDs used in this study, k_{ET} was ~$2.5\times10^{11}s^{-1}$, which is 1-2 orders of magnitude larger than $k_{r,ex}+k_{nr,ex}$ according to our recent study on the dynamics of energy transfer in Mn-doped QDs.[49,50]

The observed stronger net enhancement or net quenching of Mn luminescence compared to the exciton luminescence shown in Figure IV-3(c) can be explained with this model when the following two conditions are met: (i) exciton-Mn energy transfer is much faster than exciton relaxation ($k_{ET} \gg k_{r,ex}+k_{nr,ex}$) and (ii) the Mn excited state experiences less MNP-induced quenching than the exciton, *i.e.*, $P_{Q,Mn}(d) > P_{Q,ex}(d)$. The first condition is readily met in the doped QDs used in this study as mentioned above. The second condition is expected to be satisfied because of the weaker donor-acceptor spectral overlap of Mn-MNP pair than in exciton-MNP pair if the dominant quenching mechanism involves energy transfer to the localized surface plasmon of Ag MNP. When these two conditions are met, it follows that $R_{ET} < R_{Q,Mn} < R_{Q,ex}$ if the quenching mechanism is the same for both Mn and exciton luminescence, *i.e.*, $n=n'$. The

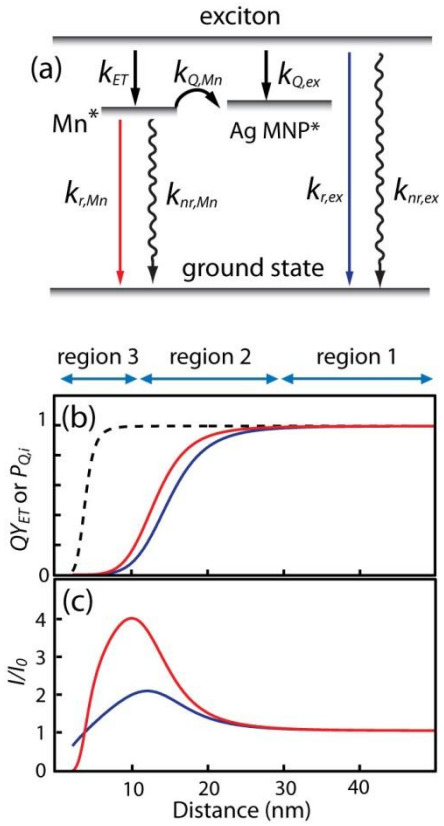

Figure IV–4. (a) Kinetic scheme of the photophysical processes in Mn-doped QD adjacent to Ag MNP. (b) *d*-dependence of QY_{ET} (dashed), $P_{Q,Mn}$ (red) and $P_{Q,ex}$ (blue) in Eq. 1 and 2. See the text for the parameters used for this plot. (c) *d*-dependence of I/I_0 for Mn (red) and exciton (blue) luminescence calculated from Eq. 1 and 2 using the same set of parameters used in (b).

corresponding distance dependence of QY_{ET}, $P_{Q,Mn}$, $P_{Q,ex}$ and the resulting I/I_0 are shown in Figure IV-4(b) and (c) respectively. The curves in these plots were calculated with the following set of parameters for the qualitative comparison with the experimental data rather than showing the fit to the experimentally measured I/I_0: R_{ET} = 3.7 nm, $R_{Q,Mn}$ = 13 nm, $R_{Q,ex}$ = 14.8 nm, $n = n' = 6$. The details of the choice of the parameters in this analysis and the limitation of the model are described in the Supporting Information.

Below we examine the different distance dependence of I/I_0 for exciton and Mn luminescence in more detail. At large QD-MNP distances (region 1), where the quenching is negligible compared to the other competing processes, both $P_{Q,ex}$ and $P_{Q,Mn}$ are close to 1. QY_{ET} is also close to 1 in this regime since $k_{ET} \gg k_{Q,ex}$. Therefore, both exciton and Mn luminescence exhibit similar I/I_0, which is slightly larger than 1. At shorter QD-MNP distances, where the quenching is not negligible, I/I_0 of the Mn and exciton luminescence will behave differently depending on the relative magnitudes of $P_{Q,ex}$ and $QY_{ET} \cdot P_{Q,Mn}$. At intermediate QD-MNP distances (region 2), where QY_{ET} is still close to 1, the Mn luminescence can take maximum advantage of the plasmon-enhanced excitation and the comparatively weaker luminescence quenching to that of the exciton. The experimentally observed behavior in Figure IV-3(c) near t = 9 nm belongs to this regime. As the QD-MNP distance continues to decrease (region 3), the rapid drop in QY_{ET} offsets the advantage of the weaker quenching of Mn, eventually leading to stronger net luminescence quenching of the Mn than the exciton. Such behavior is observed in Figure IV-3(c) at $t < 2$ nm. The model described by Eq. 21 and 22 successfully describes the observation qualitatively. On the other hand, this model overestimates the dependence of I/I_0 on the thickness of the spacer layer, since it does not account for the distribution of the QD-MNP inter-particle distances inherent in the multilayer structures used in this study (See Supporting Information). The distribution of the QD-MNP distances partially smears out the distance dependence of I/I_0, which results in the less pronounced dependence of the experimentally measured I/I_0 on the spacer layer thickness than the model predicts. The above analysis suggests that other

donor-acceptor systems exhibiting sensitized luminescence from a sufficiently fast energy transfer may also benefit from the reduced MNP-induced quenching. In the case of the Mn-doped QDs, such a benefit has more practical significance, since the Mn luminescence is often stronger and more robust than exciton luminescence even without the plasmon enhancement.[23,110]

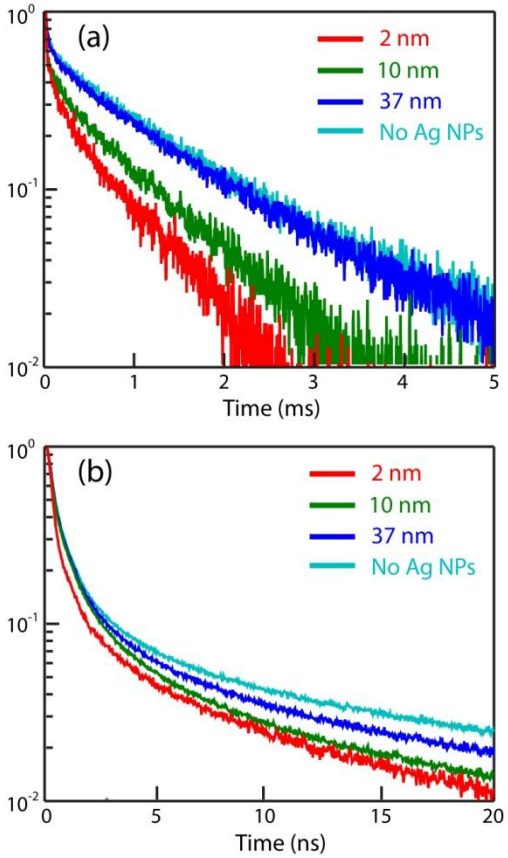

Figure IV–5. Time-resolved (a) Mn and (b) exciton luminescence intensity at various polymer spacer layer thicknesses.

We also attempted to gain further insights into the difference in MNP quenching of exciton and Mn luminescence by measuring the time-resolved luminescence intensities as a function of the spacer layer thickness (*t*). Figure IV-5(a) and (b) show the

Table IV-1. Average luminescence lifetime of exciton (τ_{ex}) and Mn (τ_{Mn}) from the undoped and Mn-doped QDs respectively at varying spacer layer thicknesses (*t*)

t	**τ_{ex}(ns)**	**τ_{Mn}(ms)**
No Ag MNP[a]	17.41	1.91
37 nm	16.68	1.78
10 nm	12.88	1.22
2 nm	4.78	0.96

[a] *Lifetime measured on Si substrates without underlying Ag MNP layer*

semi-log plots of the normalized time-resolved Mn and exciton luminescence intensities respectively at varying values of *t*. For this measurement, the entire area of the Si substrate was covered with Ag MNPs and the rest of the multilayer structure was fabricated identically to the one shown in Figure IV-1(a). The average lifetime decreases with the decrease of the spacer layer thickness for both exciton (τ_{ex}) and Mn (τ_{Mn}) luminescence as summarized in Table IV-1. Both τ_{ex} and τ_{Mn} exhibit a comparable relative decrease as the spacer layer thickness changes from t = 37 nm to 10 nm. On the other hand, τ_{Mn} decreases significantly less than τ_{ex} at t = 2 nm. This indicates that the quenching effect of Ag MNP on luminescence is weaker in Mn than for the exciton at this spacer layer thickness, consistent with our expectation. However, it is not straightforward to quantitatively measure the quenching kinetics as a function of QD-MNP distance from the time-resolved luminescence data obtained from the multilayer structure due to the heterogeneity of the quenching kinetics. There are two main sources

of the heterogeneity influencing the MNP-induced quenching kinetics in the multilayer structure used in this study. One is the distribution of QD-MNP inter-particle distances (d) for a given spacer layer thickness (t) as discussed earlier. The other is the migration of the emitting states within the QD layer, which is unequal between the exciton and Mn excited states. Excitons in undoped QDs can migrate away from the initial excitation site via inter-particle Förster resonance energy transfer (FRET) in relatively close-packed QD layer.[89,111-113] This can distort the distance dependence of the quenching kinetics especially when the Ag MNP layer is not close packed. The comparison of the time-resolved exciton luminescence in both solution and film samples indicate that interparticle FRET in the layer of QD film occurs on ~ns time scale[89,114] (see Supporting Information). Trapping of exciton by various different trap sites at different energy levels adds an additional complexity to the interpretation of time-dependent luminescence data. The trapping of exciton and thermal detrapping result in multi-exponential decay of luminescence and often responsible for a slow decay component in time-resolved luminescence data since the detrapping of exciton acts as the slowly leaking source of exciton luminescence. Such complexity also makes it difficult to define a single average lifetime of exciton that can readily be used in the evaluation of the quantum yield that usually assumes the competition among the first-order (single exponential) processes. On the other hand, the Mn excited state is highly localized on the Mn^{2+} ion and stays within the initially excited QD due to very rapid exciton-Mn energy transfer.[115] The fact that the solution and dense film samples of Mn-doped QDs exhibit the identical luminescence decay indicates the absence of migration of the Mn

excited state via FRET. Studies of isolated QD-MNP pairs with known inter-particle distances are needed to obtain more accurate kinetic information.

One interesting observation from the time-resolved luminescence measurements is that MNP-induced quenching of the Mn luminescence is still quite substantial, while it is weaker than in the exciton luminescence. Since the spectral overlap integral J of Mn-Ag MNP is two orders of magnitude smaller than that of the exciton-Ag MNP, $R_{Q,Mn}$ should be approximately half of $R_{Q,ex}$ assuming the quenching of luminescence via FRET, where the Förster distance is proportional to $J^{1/6}$.[116] In this case, Eq. 21 and 22 predict a much stronger suppression of the Mn luminescence quenching than was observed experimentally. This suggests that an additional quenching mechanism that is less sensitive to the donor-acceptor spectral overlap integral, such as quenching via electron-hole excitation near the Fermi level, may be partially involved in quenching of Mn luminescence.[109]

4.3 Conclusions

In this study, we showed that sensitized Mn luminescence arising from the fast exciton-dopant energy transfer occurring on a few ps time scale exhibits a stronger plasmon-enhancement of luminescence than the exciton due to a suppression of MNP-induced quenching of the luminescence. The rapid energy transfer that separates the absorber (exciton) and emitter (Mn) in time can partially separate the plasmon-enhancement of the excitation from the MNP-induced quenching processes, both of which results from the presence of the plasmonic MNPs. When combined with the

reduced spectral overlap between the sensitized Mn luminescence and MNP plasmon, as compared to the exciton luminescence, the Mn luminescence in Mn-doped QDs exhibited a stronger net plasmon enhancement than the exciton at the optimum separation between the MNP and QD layers.

4.4 Experimental Section

4.4.1 Materials Used for Synthesis of Quantum Dots

Cadmium oxide (Aldrich, ≥99.99%), sulfur (Aldrich, 99.98%), zinc stearate (Alfa Aesar, ZnO 12.5-14%), manganese(II) acetate tetrahydrate (Aldrich, ≥99%),1-octadecene (ODE) (Aldrich, 90%), oleic acid (Aldrich, 90%), oleylamine (OAm) (Aldrich, 70%), 11-mercaptoundecanoic acid (Aldrich, 95%), tetramethylammonium hydroxide pentahydrate (Sigma, ≥97%), (3-Aminopropyl)triethoxysilane (APTES) (≥98%, Sigma-Aldrich), silver nanoparticles (Sigma-Aldrich), poly(diallyldimethylammonium chloride) (PDADMAC) (Aldrich, M_W 100,000-200,000), poly(sodium 4-styrenesulfonate) (PSS) (Aldrich, Mw ~70,000)

4.4.2 Synthesis of the Mn-Doped and Undoped CdS/ZnS Core/Shell Quantum Dots

Mn-doped and undoped CdS/ZnS core/shell QDs were synthesized following previously reported procedures.[21,50,117] Briefly, the CdS core was synthesized by injecting 2.0 mL of octadecene (ODE) solution with sulfur (0.25 M) to a mixture of ODE (12.0 mL), CdO (125 mg) and oleic acid (2.02 g) at 250 °C, and growing at 240 °C. The rinsed CdS core was further coated with a ZnS shell via SILAR (Successive Ionic

Layer Adsorption and Reaction) procedure using ODE solutions of sulfur (0.25 M) and zinc stearate (0.25 M) as the precursors. Doping with Mn^{2+} ions was achieved by adding a Mn precursor (manganese acetate in oleylamine) at the chosen step during the SILAR process. In this study, Mn^{2+} ions were doped at the interface of the CdS core (1.8 nm in radius) and ZnS shell (1.8 nm in thickness). Since the cation and anion layers are added sequentially, the step at which the Mn precursor is introduced determines the radial location of the dopant. Details of the doping procedure can be found elsewhere.[50] In order to make the water-soluble QDs required for the deposition of the QD layer from the aqueous solution, ligand exchange was performed to replace the original surfactant with mercaptoundecanoic acid (MUA). The ligand exchange was performed by adding the QDs into a mixture of methanol, acetone and MUA at pH of 10 adjusted with tetramethylammonium hydroxide. The resulting MUA-passivated QDs were precipitated and rinsed with a 1:1 mixture of ethyl acetate and petroleum ether before finally redispersed in Millipore water. The Mn-doped and undoped CdS/ZnS core/shell QDs are shown in Figure IV-6 (a)-(d).

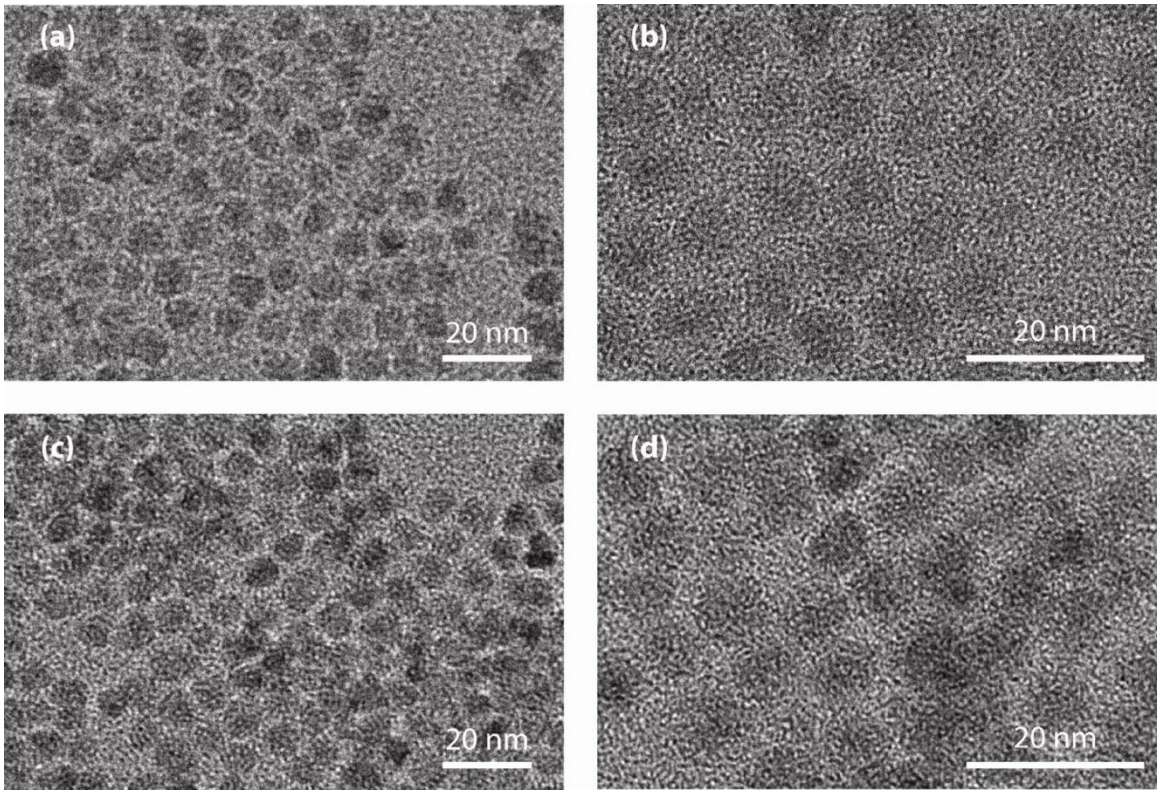

Figure IV–6. TEM images of the undoped and the Mn-doped CdS/ZnS QDs. Magnification is (a) 100k and (b) 250k of the undoped QDs, and (c) 100k and (d) 250k of the Mn-doped QDs.

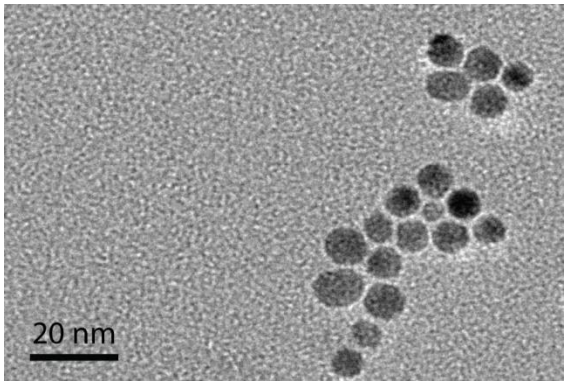

Figure IV–7. TEM image of the Ag nanoparticles.

4.4.3 Fabrication and Characterization of the Multilayered Structure on the Ag MNP-Patterned Substrate.

Clean Si (111) substrates were prepared by immersing the wafer in piranha solution at 100 °C for 1 hr and rinsing with Millipore water. To make the stripe-patterned layer of (3-aminopropyl)triethoxysilane (APTES) used as the linker between the substrate and Ag MNPs, microcontact printing method was used.[97] The polydimethylsiloxane (PDMS) stamps used for this purpose were made using a Si template having 12 μm-wide stripe patterns with a pitch of 9 μm. The inking of PDMS stamp with APTES was done by dropping 1% aqueous solution of APTES on top of the stamp. After removing the excess APTES solution with dry nitrogen from the PDMS stamp, a patterned APTES layer was transferred to the Si substrate by making a direct contact between the stamp and the substrate. The APTES-patterned Si substrate was dried for 1 hr and subsequently immersed in the aqueous solution of Ag MNPs (Sigma-Aldrich, 10 nm in diameter shown in Figure IV-7) for 45 min to allow the selective adsorption of Ag MNPs to the APTES-coated region. After rinsing the substrate with Millipore water, the resulting structure on the Si substrates were patterned stripes of Ag MNPs. A representative topographic image of the patterned Ag MNP layer on Si substrate obtained with an atomic force microscope (AFM, Agilent Technologies 5500) is shown in Figure IV-1(b). The polyelectrolyte spacer layer that separates the Ag MNP layer and QD layer was formed on top of Ag MNP layer using a layer-by-layer deposition method.[46,77] Oppositely charged layers of poly(diallyldimethylammonium chloride) and poly(sodium 4-styrenesulfonate) were alternately deposited from 0.5 M

NaCl solutions of the polyelectrolyte. The thickness of the spacer layer was changed by varying the total number of layers deposited. The thickness of the spacer layer was measured from the topographic AFM images of the covered vs. uncovered regions of the substrate obtained with a WITec Alpha 300 AFM. The roughness of the polyelectrolyte layer surface in AFM image is ~ ±1 nm, while the actual surface roughness could be larger due to the finite lateral dimension of the AFM tip. The QD layer was deposited on top of the outermost spacer layer by dipping the substrate in the aqueous solution of 1:1 mixture of Mn-doped and undoped QDs for ~1 min and rinsing the substrate thoroughly with Millipore water. All AFM images were acquired under ambient conditions in tapping mode using commercially available aluminum-coated silicon AFM tips from Nanoscience Instrument (Phoenix, AZ) with nominal tip radii of less than 10 nm and nominal spring constants of 48 N/m.

4.4.4 Measurements of Spacer Layer Thickness and Distribution of QD-Ag MNP Inter-Particle Distances Distribution

The thickness of the polymer spacer layer separating Ag MNP and QD layers on Si substrate was obtained by measuring the step height in the scratched Si substrates that have Ag MNPs and the spacer layers with AFM. Figure IV-8 show the AFM image of Si substrate with Ag MNPs (10 nm diameter) only. Figure IV-9 shows the height profile of the polymer layer on deposited Si substrate measured with tapping-mode AFM after scratching the substrates. A close inspection of Figure IV-8 indicates that the nearest-neighbor distance between Ag MNPs is ~50 nm. The relatively large inter-particle

distance compared to the particle size (10 nm) is due to the repulsion of the negatively charged Ag MNPs passivated with citrate. Because of the non-close packed Ag MNP layer, the nearest QD-Ag MNP inter-particle distance has a distribution that varies with the spacer layer thickness. The distribution is wider for shorter spacer layer thickness.

Figure IV-10 illustrates the distribution of the nearest center-to-center distance between QD and Ag MNP calculated with a model layer structure at two different spacer layer thicknesses. The model layered structure for this calculation is composed of a cubic closed-packed layer of QDs (QD+surfactant radius=4 nm) and one Ag MNP (radius=5nm) at the center of 50×50 nm^2 square area.

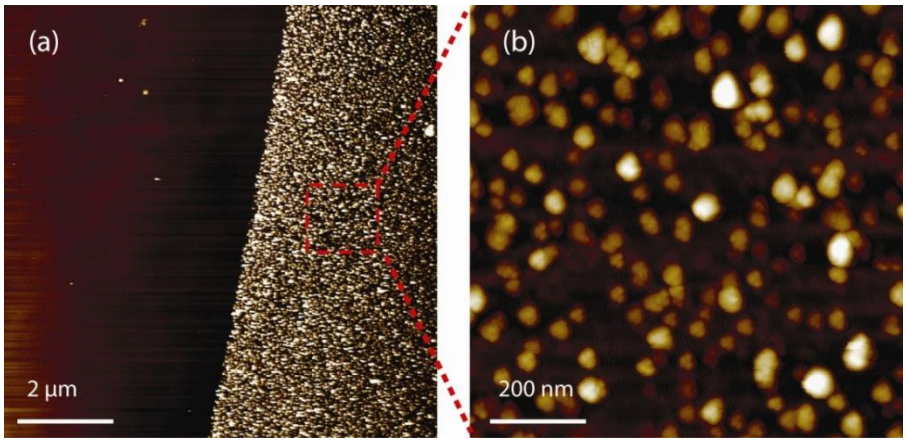

Figure IV–8. AFM images of the Si substrate with the patterned Ag MNPs (a) 9×9 μm^2, (b) 1×1 μm^2 area.

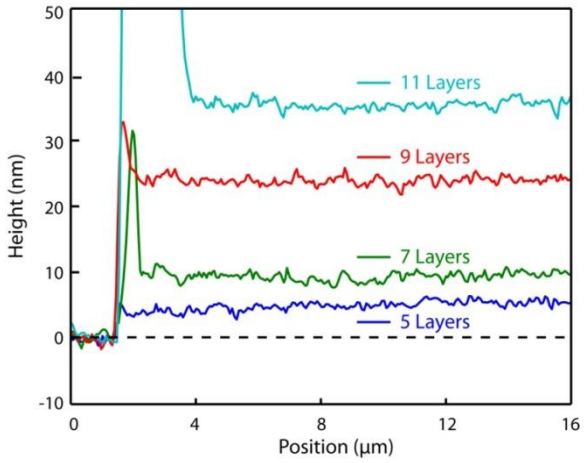

Figure IV–9. The height profile of the polymer spacer layers on the scratched Si substrate measured with tapping-mode AFM.

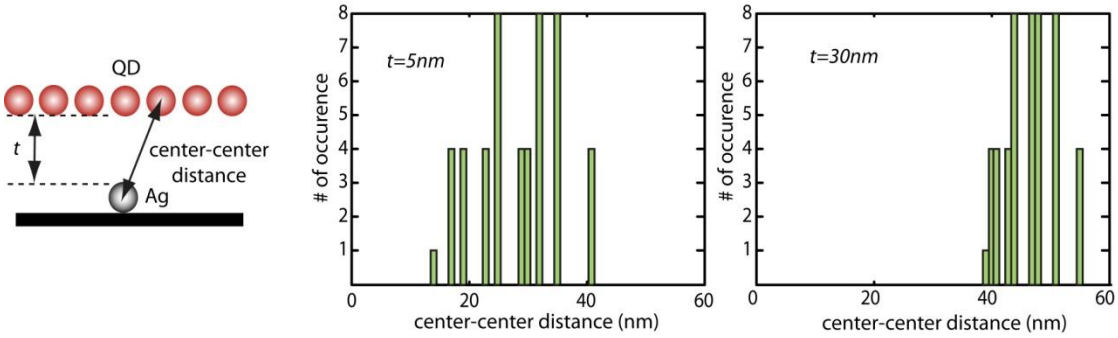

Figure IV–10. Calculated distribution of center-to-center distances between QD and Ag MNP.

4.4.5 Imaging of Plasmon-Enhanced Luminescence Intensity on the Patterned Structure

Optical setup for the imaging of luminescence is shown in Figure IV-11. The microscope used for imaging the luminescence from was constructed using the Cage System (Thorlabs) directly on a bread board ('1x4' foot print). The image was collected with a 50X objective lens (Nikon, CFI L Plan EPI SLWD) and focused onto on a liquid nitrogen-cooled CCD camera (Princeton Instrument, PI-LCX) with a tube lens (Nikon,

focal length=200 mm). The sample stage was mounted on an xyz translation stage with piezo actuators (Newfocus, Picometer). The sample was illuminated with a 405 nm diode laser. A clean-up filter (Semrock, LD01-405/10) was used to remove the unwanted wavelength component from the excitation light. A neutral density filter was placed before the sample to adjust the intensity of the excitation light. A combination of a longpass filter (410 nm, F1) and a bandpass filter (F2) was used to selectively image either exciton or Mn luminescence. 450 nm and 600 nm bandpass filters have fwhm of 60 nm and 10 nm respectively.

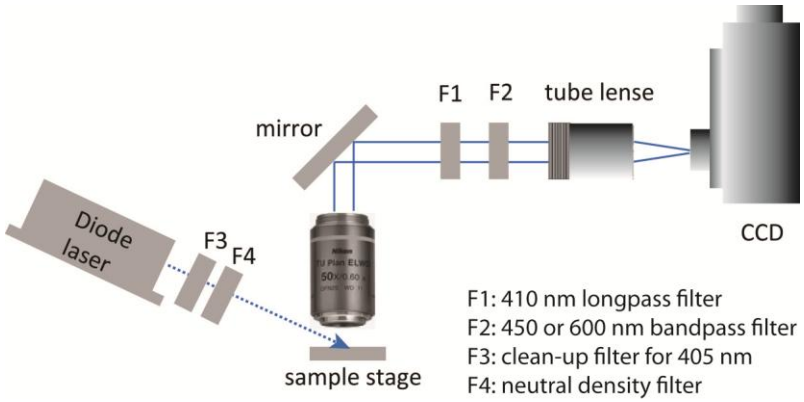

Figure IV–11. Optical setup for the imaging of luminescence

4.4.6 Time-Resolved Luminescence Intensity Measurements

The time-resolved luminescence was measured using two different methods. For the Mn luminescence, a pulsed nitrogen laser (Stanford Research Systems, NL100, 3.5 ns pulse width) centered at 337 nm and photomultiplier tube (Hamamatsu, 982R) were used in conjunction with a digital oscilloscope (LeCroy, WaveAce). A 500 nm longpass

filter was used to prevent the excitation light reaching the detector. For the exciton luminescence, a time-correlated single photon counting (TCSPC) technique was used to measure the time-resolved luminescence. A pulsed diode laser (Picoquant, 80 ps pulse width) centered at 405 nm operating at 10 MHz was used as the excitation source. The exciton luminescence filtered with 450 nm bandpass filter (fwhm = 50 nm) was detected with a TCSPC-enabled PMT, with channel binning of 32 ps over the full time window (100 ns) of the measurement. The time-resolved exciton luminescence was obtained at several different areas on the substrate on a confocal microscope (Olympus, FV-1000) using a fluorescence life time imaging (FLIM) technique. The average lifetimes (τ_{avg}) reported in Table IV-1 are $\tau_{avg} = \sum(a_i \cdot \tau_i^2)/\sum(a_i \cdot \tau_i)$, where a_i and τ_i are the amplitude and time constant obtained from the multi-exponential fit of the data.

4.4.7 Comparison of the Time-Resolved Luminescence Intensity between the Dilute Solution and the Thin Film Sample

Figure IV-12(a) compares the time-resolved Mn luminescence intensities of Mn-doped QDs measured from dilute solution and film formed on a Si substrate. Figure IV-12(b) shows the same comparison made for the exciton luminescence of undoped QDs. Mn luminescence exhibits nearly identical decay of the luminescence intensity in both solution and thin film samples. Exciton luminescence decays more rapidly in thin film sample compared to the solution sample and considered due to the inter-particle energy transfer.[89,114]

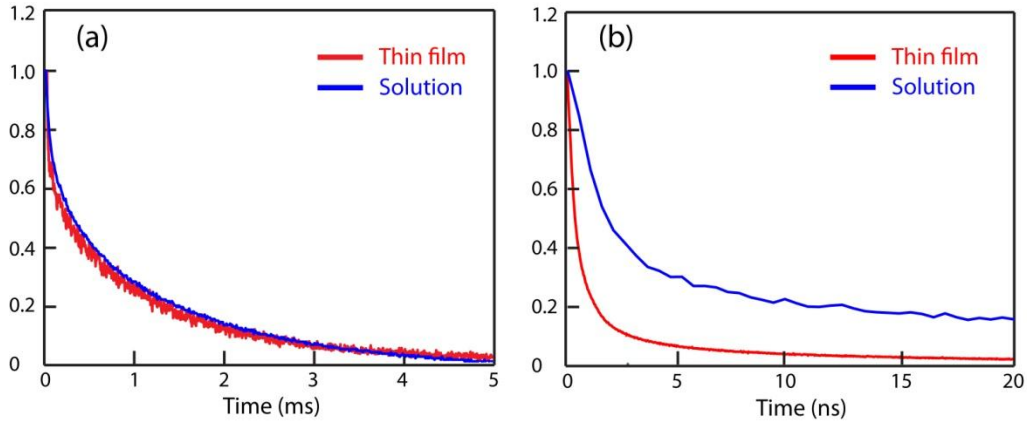

Figure IV–12. Time-resolved (a) Mn and (b) exciton luminescence intensity from the dilute solution and the dropcast thin film sample.

4.4.8 Test of the Effect of the Multilayered Structure (Polyelectrolyte Layer/Ag MNP/APTES/Si Substrate) on the Collection Efficiency at Different Wavelengths.

The effect of the multilayered structure (polyelectrolytes/with or without Ag MNP/APTES/Si substrate) on the collection efficiency due to reflection/scattering from the construct was compared at two different collection wavelengths of 450 and 600 nm. A monochromator was used to select the specific wavelength from a white light source, and a CCD camera was used to image the scattered/reflected light from the construct. Four different images were taken as shown in Figure IV-13(a)-(d), and Figure IV-13 (e) was taken as the region of interest (ROI) from the ratio image of ($I_{layer,450}$ / $I_{bare,450}$)/($I_{layer,600}$/ $I_{bare,600}$). The average value of the ratio in ROI is 1.01 which indicates that the presence of the multilayered structure has the equal effect on the overall photon collection efficiency of the exciton and Mn luminescence.

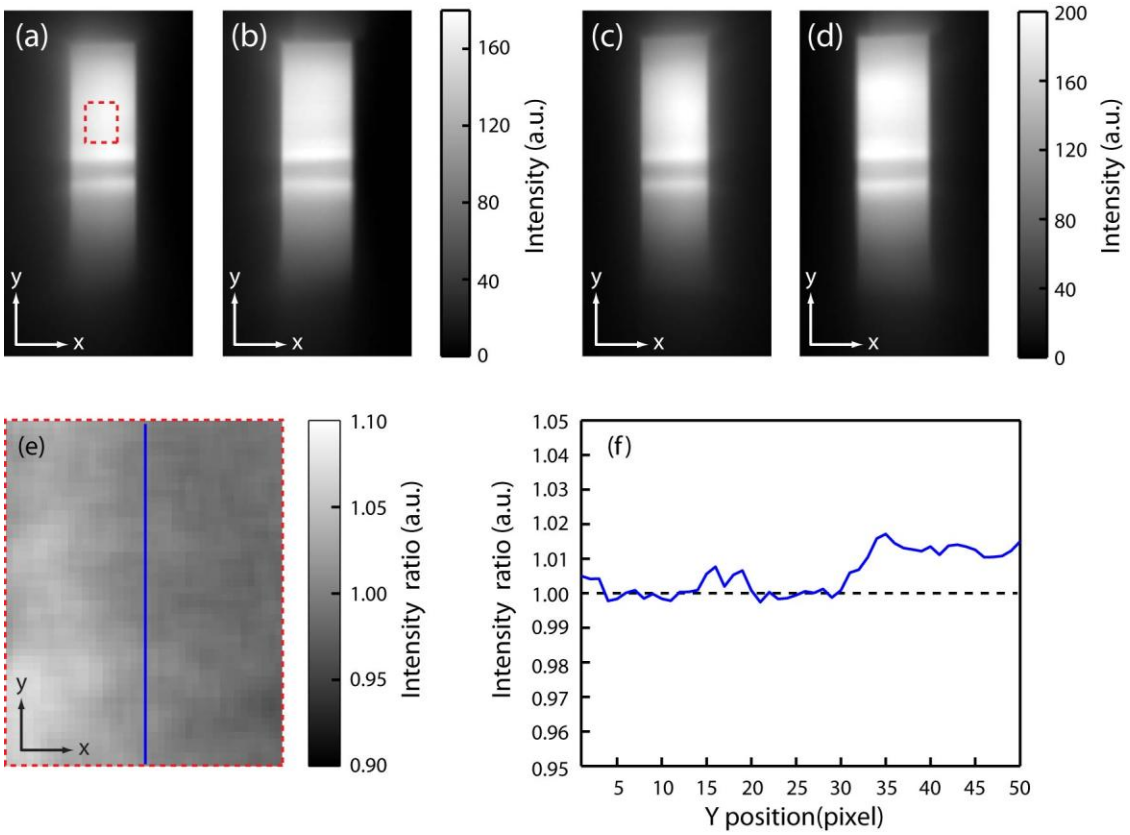

Figure IV–13. (a)-(d) Images of scattered/reflected light projected on the same construct (polyelectrolytes/with or without Ag NPs/APTES/Si substrate) at two different wavelengths (450 and 600 nm), (a) with Ag NPs at 450 nm ($I_{layer,450}$), (b) without Ag NPs at 450 nm ($I_{bare,450}$), (c) with Ag NPs at 600 nm ($I_{layer,600}$), (d) without Ag NPs at 600 nm ($I_{bare,600}$). (e) The region of interest (red dotted line shown in (a)) in the ratio image of ($I_{layer,450}/I_{bare,450}$)/ ($I_{layer,600}/I_{bare,600}$) and (f) the cross section in (e) (blue solid line).

4.4.9 Modeling *d*-Dependence of Plasmon-Enhanced Luminescence

d-dependence of the plasmon-enhanced luminescence, $I(d)/I_0$, was described using the following equations. $P_{E,ex}$ is the excitation enhancement factor, $P_{Q,ex}$ and $P_{Q,Mn}$ are the quenching factor for exciton and Mn luminescence, and QY_{ET} is the quantum yield of exciton-Mn energy transfer in the presence of Ag MNP.

$$I_{ex}(d)/I_0 = P_{E,ex}(d) \cdot P_{Q,ex}(d) = P_{E,ex}(d) \cdot \left(\frac{k_{r,ex} + k_{nr,ex}}{k_{r,ex} + k_{nr,ex} + k_{Q,ex}(d)} \right)$$

$$= \left(\left(\frac{R_E}{d}\right)^{n_E} + 1\right) \cdot \left(\frac{1}{1 + \left(R_{Q,ex}/d\right)^{n}}\right) \quad (23)$$

$$I_{Mn}(d)/I_0 = P_{E,ex}(d) \cdot QY_{ET}(d) \cdot P_{Q,Mn}(d)$$

$$= \left(\left(\frac{R_E}{d}\right)^{n_E} + 1\right) \cdot \left(\frac{k_{ET}}{k_{r,ex} + k_{nr,ex} + k_{Q,ex}(d) + k_{ET}}\right) \cdot \left(\frac{k_{r,Mn} + k_{nr,Mn}}{k_{r,Mn} + k_{nr,Mn} + k_{Q,Mn}(d)}\right)$$

$$\approx \left(\left(\frac{R_E}{d}\right)^{n_E} + 1\right) \cdot \left(\frac{k_{ET}}{k_{Q,ex}(d) + k_{ET}}\right) \cdot \left(\frac{k_{r,Mn} + k_{nr,Mn}}{k_{r,Mn} + k_{nr,Mn} + k_{Q,Mn}(d)}\right)$$

$$= \left(\left(\frac{R_E}{d}\right)^{n_E} + 1\right) \cdot \left(\frac{1}{1 + (R_{ET}/d)^{n}}\right) \cdot \left(\frac{1}{1 + \left(R_{Q,Mn}/d\right)^{n'}}\right) \quad (24)$$

$k_{r,i}$: radiative relaxation in the absence of MNP for exciton (i=*ex*) and Mn (i=*Mn*)
$k_{nr,i}$: nonradiative relaxation in the absence of MNP for exciton (i=*ex*) and Mn (i=*Mn*)
$k_{Q,i}$ (d): MNP-induced quenching of luminescence for exciton (i=*ex*) andMn (i=*Mn*)
k_{ET}: exciton-Mn energy transfer rate

Following parameters were used for the plots in Figure IV-4(b). For the excitation enhancement factor and exciton quenching factor, R_E =17.7 nm, n_E=5.3, $R_{Q,ex}$=14.8 nm and n=6 were used, which were taken from our earlier study on a related system.[77] R_{ET} was estimated to be ~3.7 nm using Eq. 23 from the rate constants of exciton relaxation in undoped QDs ($k_{r,ex}+k_{nr,ex} \approx 5.7 \cdot 10^7 s^{-1}$) and the energy transfer in doped QDs ($k_{ET} \approx 2.5 \cdot 10^{11} s^{-1}$) with n=6. We chose $R_{Q,Mn}$=13 nm, since it well-illustrates qualitatively the difference in d-dependence of $I(d)/I_0$ between exciton and Mn luminescence observed in the experiment. Because of the distribution of QD-MNP inter-

particle distance in thin film structure and other heterogeneity described in the text, the model based on the Eq. 23- 25 will have a limited quantitative validity.

$$\frac{\left(R_{Q,ex}/d\right)^n}{(R_{ET}/d)^n} = \frac{\left(\frac{k_{Q,ex}\,(d)}{k_{r,ex}+k_{nr,ex}}\right)}{\left(\frac{k_{Q,ex}\,(d)}{k_{ET}}\right)},$$

$$\frac{R_{Q,ex}}{R_{ET}} = \left(\frac{k_{ET}}{k_{r,ex}+k_{nr,ex}}\right)^{\frac{1}{n}} \tag{25}$$

CHAPTER V

RATIOMETRIC TEMPERATURE IMAGING USING ENVIRONMENT-INSENSITIVE LUMINESCENCE OF MN-DOPED CORE/SHELL NANOCRYSTALS*

5.1 Introduction

Recent progress in luminescence thermometry using temperature-dependent luminescence of various molecular and nanocrystalline materials made it possible to measure the temperature optically with high accuracy (<0.1 ºC) and spatial resolution (<10 μm).[51-62]

The luminescence thermometry has been applied to the temperature sensing of various platforms such as micro/nanofluidics, integrated devices and intracellular environment.[81-86] Temperature dependence of the intensity, spectral position, bandwidth, polarization and lifetime of the luminescence are among the frequently utilized temperature sensing mechanisms in luminescence thermometry.[53-56] Therefore, the insensitivity of these characteristics of luminescence to the other variables besides the temperature is very important for the accurate and reliable temperature sensing.[64,84,118] However, the luminescence of many materials utilized for temperature sensing is often affected by the variation of the surrounding chemical environment at a given

---

*Reprinted in part with permission from Park, Yerok; Koo, Chiwan; Chen, Hsiang-Yun.; Han, Arum; Son, Dong Hee. Ratiometric Temperature Imaging Using Environment-Insensitive Luminescence of Mn-Doped Core–Shell Nanocrystals. *Nanoscale* **2013,** 5, 4944-4950. Copyright 2013 by the Royal Society of Chemistry.

temperature. For instance, luminescence intensity and peak position of many thermo-sensitive dye molecules vary significantly as the polarity or pH of the surrounding medium changes.[63,64] The lifetime of the luminescence can also be influenced by the surrounding medium interfering with the temperature measurement.[52,65] In the case of quantum dots, the variation of the surface functionalization and interparticle distance can change the exciton luminescence intensity and spectrum.[87-89]

One strategy that was shown to be effective in reducing the environmental sensitivity of the luminescence thermometry is to coat the temperature-sensing material with 'shell' material that forms a barrier between the sensor and the surrounding medium. For instance, a thick polymer layer formed on the thermosensitive fluorescent dye-imbedded nanoparticles effectively reduced the sensitivity of the luminescence lifetime to the variation of pH and ionic strength, enabling more reliable temperature sensing.[119] In the case of the thermometry based on the luminescence intensity, ratiometric measurement of the multiple emitters has become more common recently, where the temperature-dependent ratio of the two different luminescence intensities is measured instead of the absolute intensity. The dual emitting materials used for such purpose include lanthanide-codoped nanoparticles or metal-organic framework (two dopant emissions) and Mn-doped quantum dot (exciton and dopant emissions).[57-61] Since the intensity ratio fluctuates much less than the absolute intensity, the ratiometric thermometry is generally more accurate than non-ratiometric methods for the optical temperature imaging.

While the ratiometry allows more robust intensity-based luminescence

thermometry, the environmental sensitivity still remains as a challenging issue due to the potentially unequal effect of the surrounding environment on the intensities of the different emitters. For instance, the luminescence intensities of exciton and dopant in nanocrystals are affected differently by the charge carrier-accepting molecules (e.g., thiols) or the dissolved oxygen present in the surrounding medium depending on the spatial proximity of the emitter and the molecules affecting the luminescence.[90,91]

Here, the ratiometric surface-temperature imaging of a cryo-cooling device in a wide temperature range (77−260 K) is demonstrated by using Mn luminescence from Mn-doped CdS/ZnS core/shell nanocrystals with controlled host structure and doping location, which is highly insensitive to the surrounding chemical environment and exhibits near-linear temperature response in a broad range of temperatures (100−380 K). The diminished sensitivity of the method reported here to the environmental variation is ascribed to the use of 'single' luminescence from Mn^{2+} ions doped far below the surface of the nanocrystals (~2.1 nm) with controlled doping radius, whose spectral lineshape is highly insensitive to the environment outside of the nanocrystals. For the same reason, high quantum yield of luminescence can be maintained even under the conditions that are known to significantly diminish the exciton luminescence. The broad bandwidth (~90 nm at 293 K) and robust Mn luminescence spectrum enable the ratiometric thermometry even with a single luminescing species, i.e., Mn^{2+} ions. The temperature sensitivity ($\Delta I_R/I_R$ = ~0.5%/K at 293 K, I_R = intensity ratio) in a wide range of temperatures was obtained by controlling the local lattice strain at the dopant site, which significantly enhances the bandwidth broadening and peak shift with temperature

increase.[26,95] Since only a single emitting species is used, the issue of potentially different effect of the surrounding environment on different emitters is avoided. Here, we performed the ratiometric surface temperature imaging of a glass substrate partially exposed to the liquid nitrogen to demonstrate the capability of the reliable thermometer in a wide range of temperatures. Despite the inhomogeneity of the nanocrystal coating formed on the substrate via spin coating, the surface temperature ranging from 77 to 260 K could be reliably imaged on a CCD camera thanks to the environmental insensitivity of Mn luminescence and large dynamic range of temperature sensing. The ratiometric temperature imaging with Mn-doped CdS/ZnS nanocrystals demonstrated in this study will be particularly useful for the optical surface-temperature imaging of the chemically heterogeneous system with a large distribution of temperatures.

5.2 Results and Discussion

Figure V-1(a) shows the luminescence spectra of Mn-doped CdS/ZnS core/shell nanocrystals (NCs) used in this study in the temperature range of 77 to 380 K. The Mn^{2+} ions are doped at the interface between the CdS core (3.6 nm in diameter) and the ZnS shell (2.1 nm in thickness) at the average doping concentration of ~45/particle determined from the elemental analysis. The two dashed curves in Figure V-1(a) are the transmittance spectra of the bandpass filters centred at 600 and 650 nm used for the ratiometric temperature imaging in this study. These two wavelengths are chosen since the ratio of the intensities exhibit a large usable linear dynamic and the simple bandpass filter can readily separate them spectrally. Figure V-1(b) shows the ratio of the

intensities ($I_R = I_{600}/I_{650}$) measured with the two band-pass filters in the temperature range of 77−380 K normalized to the intensity ratio (I_R) at 293 K, which serves as the temperature calibration curve. Near the ambient temperature, I_R varies at the rate of 0.5%/K.

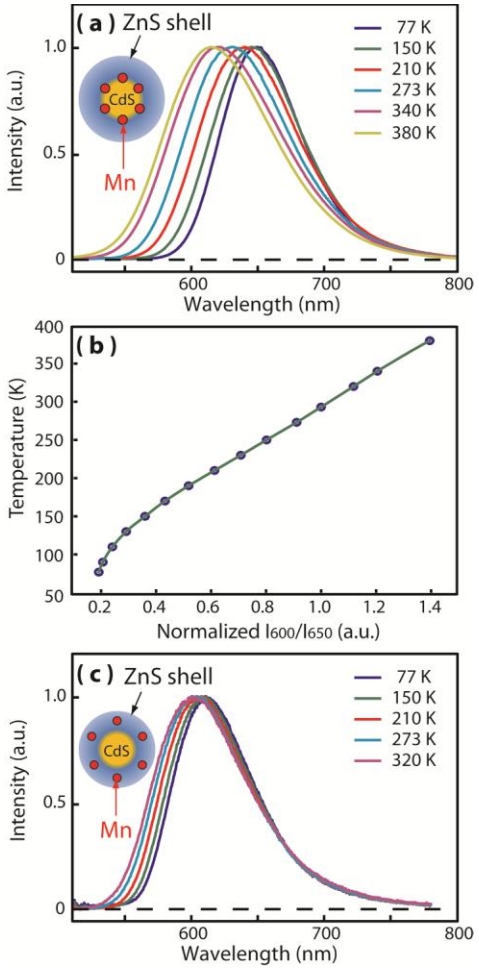

Figure V–1. (a) Normalized Mn luminescence spectra of Mn-doped (at the interface between the CdS core and ZnS shell) NCs with high local lattice strain at Mn^{2+} sites used for thermometry in this study. (b) Intensity ratio of I_{600}/I_{650} at different temperatures (blue dots: experimental data, green line: interpolation curve). (c) Normalized Mn luminescence spectra of typical Mn-doped (in the ZnS shell) NCs with weak local lattice strain at Mn^{2+} ion sites. Insets in (a) and (c) pictorially represent the structures of Mn-doped core/shell NCs with different radial doping locations.

The structure of the NCs used in this study was specifically controlled to enhance the temperature dependence of the bandwidth and peak position. Our recent study indicated that the local lattice strain at Mn^{2+} sites softens the vibrational mode coupled to Mn luminescence and increases local thermal expansion, which results in a significant enhancement of the bandwidth broadening and peak shift with the temperature increase.[26] The local lattice strain arises from the lattice mismatch between the core and shell, which increases as it gets closer to the core/shell interface. In the NCs used in this study, the local lattice strain on Mn^{2+} ions was maximized by doping at CdS/ZnS interface employing SILAR (Successive Ionic Layer Adsorption And Reaction) method to maximize the temperature dependence of Mn luminescence. For comparison, significantly weaker temperature dependence of Mn luminescence spectra from Mn-doped NCs, where Mn^{2+} ions are doped at low-strain region in the ZnS shell, is shown in Figure V-2(c). Since the diffusion of Mn^{2+} ions within the host NC is negligible below <400 K, the structurally optimized temperature dependence of Mn luminescence spectrum is maintained robustly within the temperature range of our study. Above ~500K, however, the diffusion of Mn^{2+} ions begins to become non-negligible and limits the applicability at the higher temperatures.[120,121]

In general, the ratiometric luminescence thermometry using the luminescence intensities of two emitting states is based on the Boltzmann population determined by $e^{-\Delta E/kT}$, where ΔE is the energy difference between the two emitting species. In this work, while we rely on a single emitting species (i.e., Mn^{2+} ions), the situation is similar to having a multiple number of emitting states separated by the energy of the coupled

vibrational mode, whose populations also follow the Boltzmann statistics. Because of the broadening of each vibronic transition that results in the smooth spectral lineshape, luminescence from higher-lying state appears as the broadening of the spectral lineshape. In this sense, the temperature measurement based on Mn luminescence operates on the same principle as the typical ratiometric method based on multiple emitting species. The linear increase of Mn luminescence bandwidth above ~70 K follows the functional form of $\coth(\hbar\omega/2kT)$ and the linear local thermal expansion, where ω is the frequency of the vibrational mode coupled to Mn emission.[26,95]

The potential influence of the surrounding environment on the luminescence is the common issue for the luminescence thermometry and poses a challenge in temperature sensing under the chemically heterogeneous environment such as in the biological cell.[84-86,118,119,122,123] For the fluorescence of the molecular species and the exciton fluorescence of quantum dots, both the intensity and the shape of the luminescence spectra can vary with the polarity of the surrounding medium or concentration of the fluorophore due to solvatochromism or interparticle electronic coupling.[63,89,124,125] In the case of semiconductor quantum dot, the surfactant molecules can also influence the luminescence intensity via charge carrier transfer between the surfactant and the quantum dot to a varying degree depending on the structure of the quantum dot.[126] Therefore, the potential differences in the effect of the surrounding environment on the luminescence of the different emitting species can complicate even the ratiometic temperature sensing. A common strategy that has been used to address such issue is adding a thick shell (e.g., polymer) that surrounds the sensor material and

prohibits the access of the molecules in the surrounding medium. In Mn-doped core/shell NCs used in this work, the inorganic shell (ZnS) combined with the local nature of the *d* electrons of Mn makes Mn luminescence highly insensitive to the surrounding medium even without thick polymer shell.

Figure V-2(a)-(c) exemplify the robustness of Mn luminescence spectrum with respect to the large variation of several environmental variables, such as the solvent polarity, surface-passivating molecules, concentration of the NCs and pH of aqueous medium. All the NCs used in the above comparison have ~2.1 nm of ZnS shell above Mn^{2+} ions and passivated with organic surfactants with aliphatic tail group containing 11-18 carbons. Figure V-2(a) compares the Mn luminescence spectra of the NCs at 293 K dispersed in chloroform and water that have very different polarity (ε = 4.8 vs. 80.4 for chloroform and water at 293 K respectively). The two NCs also have different surface-passivating surfactant to give the solubility in each solvent, i.e., oleic acid and 11-mercaptoundecanoic acid (MUA) for chloroform and water respectively. The bottom panel shows the difference between the two normalized spectra (ΔI) in two different solvents. Even with such extreme difference in the solvent polarity and the surface passivating functional group, the two spectra are very close with less than 1% difference introduced to the value of ΔI. (< 2 K shift in temperature). The difference of the spectra between the two different solvents with relatively small difference in polarities (e.g., hexane and toluene) is within the noise level of detection by the spectrometer.

Figure V-2(b) compares Mn luminescence spectra of the oleic acid-passivated NCs in different phases of the surrounding medium: liquid (chloroform), solid substrate

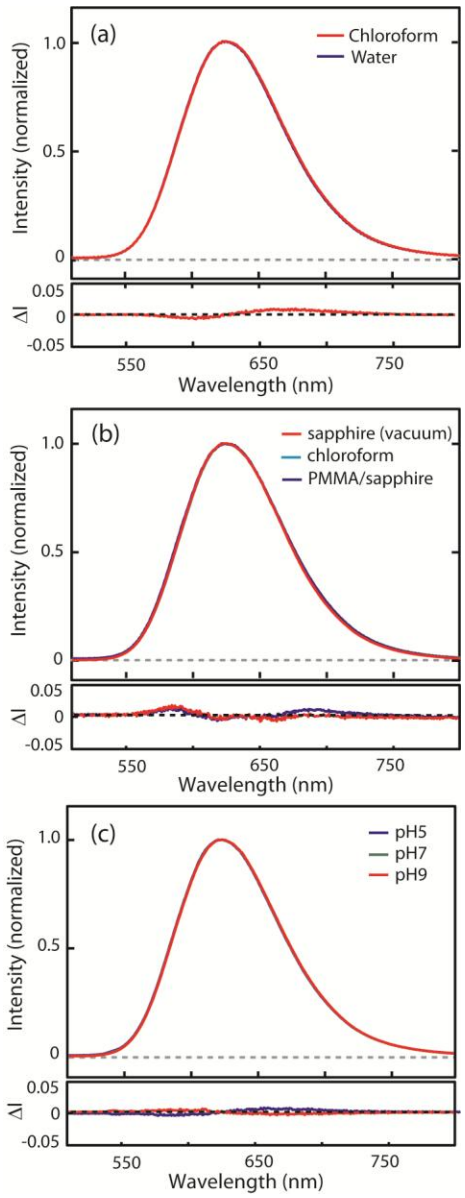

Figure V–2. Comparison of the normalized luminescence spectra of Mn-doped CdS/ZnS NCs under different medium environment. (a) Solvent dependence; chloroform (s_1) and water (s_2), (b) Medium phase dependence; on sapphire under vacuum (s_3), PMMA/sapphire (s_4), chloroform (s_1) is shown for comparison. (c) pH dependence: pH5 (s_5), pH7 (s_6) and pH9 (s_7). The bottom panels are the intensity difference of the normalized spectra. (a) s_1-s_2, (b) s_1-s_3 (blue), s_1-s_4 (red), (c) s_6-s_5 (blue), s_6-s_7 (red).

in vacuum (sapphire) and polymer film on solid substrate (PMMA/sapphire). The sample on the sapphire was prepared by drop-casting the concentrated chloroform solution of NCs and forms an aggregate of the NCs. The sample in the polymer medium was prepared by spin coating the dilute NC solution in PMMA-chloroform mixture. The difference of the spectra (blue: s_1-s_3, red: s_1-s_4) shown in the bottom panel indicates less than 1% variation in ΔI is introduced by the change of phase of the surrounding medium and aggregation. The spectra from the aggregated NCs and dispersed NCs in PMMA polymer were nearly identical within the noise of the spectrometer. Figure V-2(c) shows the pH-dependent Mn luminescence spectrum of MUA-passivated NCs. Even with the onset of partial aggregation of the NCs at pH 5, the luminescence spectra remains highly robust with less than 0.5% change in ΔI. Compared to the materials with thick (tens of nm) polymer shell that has been used to protect the temperature sensing nanoparticles, inorganic core/shell structure can provide comparable protection at much smaller sizes. For Mn-doped CdS/ZnS NCs studied here, thickening of ZnS shell or adding the polymer shell is expected to further improve the insensitivity of the luminescence spectrum to the surrounding environment.

Having established the robustness of the temperature-dependent Mn luminescence spectral lineshape with respect to the variation of the surrounding environment, we performed imaging of the surface temperature of a cryo-cooling device experiencing a large thermal gradient. Figure V-3(a) shows the structure of the device,

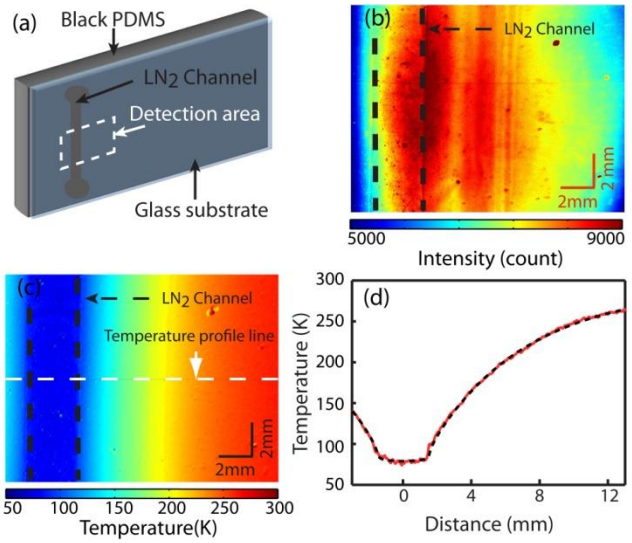

Figure V–3. (a) Schematics of the cryo-cooling device. The imaging area is indicated by the dashed rectangle. (b) Color contour plot of the intensity image (I_{650}) from the device with liquid nitrogen flow in the channel. (c) Color contour plot of the temperature converted from the intensity ratio image. (d) Temperature line profile (solid) and the simulation result (dashed) at the location indicated in (c).

where the liquid nitrogen flows in the channel formed under the glass substrate by the black poly(dimethylsiloxane) (PDMS) polymer. Such device that provides local cryo-cooling has been used in low-temperature applications, e.g., cryo magnetic resonance imaging.[127] However, the spatially-resolved temperature profile at the interface of two materials in such device could not be measured readily. To measure the temperature distribution at the interface of the glass substrate and PDMS in this study, Mn-doped NCs were spin-coated on the side of the glass substrate facing the PDMS polymer.

Figure V-3(b) and 3(c) shows the color contour plot of the raw intensity profile at 650 nm (I_{650}) and the temperature profile obtained from I_R respectively. For this measurement, the steady flow of liquid nitrogen in the channel and constant flush of dry nitrogen gas at 293 K above the surface of the glass substrate were maintained as

described in detail in the Experimental section. The ratiometric temperature imaging was performed using a CCD camera by taking the ratio of the two intensity images recorded at 600 and 650 nm. The intensity image at each wavelength was taken using the bandpass filter placed in front of the CCD with the exposure time of 20 sec. A UV LED that illuminates the area of ~5 cm^2 was used as the excitation source.

Despite the inhomogeneous NC coating and the uneven lighting condition by the LED, giving rise to a large spatial fluctuation in the absolute luminescence intensity, the measured temperature profile shows a very smooth variation. In Figure V-3(d), a line profile of the temperature at a chosen location is shown. The temperature gradient from 77 to 260 K developed over the distance of 12 mm is clearly observed. The superimposed dashed line is the result of finite element method (FEM) calculation performed with a commercially available FEM software (Comsol Multiphysics™, COMSOL Inc.) described in the Experimental section.[127] In this simulation, the effect of dry nitrogen flushing over the device was accounted for by adjusting the value of the heat transfer coefficient (h) at the glass/nitrogen interface. Using the value of $h = 40$ that corresponds to the thermal conductivity of the glass under the highly convective environment, a good agreement between the calculated and measured temperature profile is obtained. The average noise in the temperature image shown in Figure V-3(c) is ±1 K, which is mainly due to the limitation of the imaging with a CCD camera, where different area is sensed by different pixels. However, the signal to noise ratio can be improved by averaging the multiple number of images from the CCD or employing scanning imaging technique combined with more sensitive detectors.

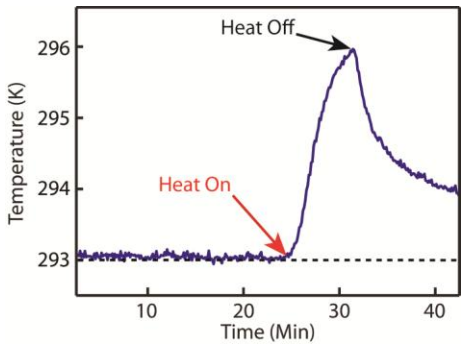

Figure V–4. The time-profile of the temperature of hexane solution of the NCs in a cuvette under the constant and varying temperature conditions. The temperature trace is converted from the luminescence intensity ratio shown in Figure V-1(b).

In order to test the stability and resolution of the temperature sensing based on Mn luminescence spectral lineshape, we measured the luminescence spectrum of a solution sample as a function of time with a CCD spectrometer instead of imaging with a CCD camera. Figure V-4 shows the temperature of the solution sample in a cuvette measured with the integration time of 100 msec at 10 sec interval. During the first 25 min, the temperature of the cuvette was kept constant. Subsequently, the temperature of the cuvette was increased by flowing warm nitrogen gas to the exterior of the cuvette. The heating of cuvette was stopped after 5 mins and the cuvette was allowed to return to the initial ambient temperature. The temperature change was detected with less than ±0.05 K of noise demonstrating the robustness and sensitivity of the temperature sensing method.

The key advantages of the temperature imaging method described here are the highly insensitive spectral lineshape of Mn luminescence with respect to the variation of the surrounding chemical environment and the wide linear dynamic range of temperature sensing. The temperature of chemically heterogeneous surface can be reliably imaged

via spin coating or spraying of the NCs. High quantum yield of Mn-doped NCs used in this study (>35%), which is maintained even with particle aggregation and thiol passivation, is another advantage over other quantum dot-based temperature sensors. A broad measurable temperature range (ΔT ~300 K) extending from cryogenic to above-ambient temperature with a linear correlation between the temperature and the measured signal will be particularly suitable for the temperature imaging a large thermal gradient, such as the device with local heating or cooling.

5.3 Conclusions

We report the ratiometric temperature imaging based on temperature-dependent Mn luminescence spectrum from Mn-doped CdS/ZnS NCs that is highly insensitive to the surrounding environment and exhibiting near-linear temperature response in a broad range of temperatures (100−380 K). The Mn luminescence from the NCs used in this study was made highly insensitive to the variation of the surrounding environment, such as the surface passivation, polarity and pH of medium, by confining Mn^{2+} ions below the shell in core/shell structure of the NC. The temperature sensitivity of the spectrum was enhanced by utilizing the local lattice strain created by the core/shell lattice mismatch that results in the stronger bandwidth broadening and peak shift with the temperature increase. Taking advantage of the weak environmental sensitivity of Mn luminescence spectrum and large temperature sensing range, we demonstrate the ratiometric temperature imaging of a cryo-cooling device. The surface temperature profile of the device ranging from 77 to 260 K was readily imaged with a CCD camera from the

luminescence of the NCs spin-coated on the surface of the substrate. The method shown here will be particularly useful for the temperature imaging of the surfaces exhibiting a wide range of temperature variation and exposed to the chemically inhomogeneous environment.

5.4. Experimental Section

5.4.1 Synthesis of Mn-Doped CdZ/ZnS Core/Shell Nanocrystals with Controlled Radial Doping Location

Mn-doped CdS/ZnS core/shell nanocrystals (NCs) with controlled radial doping location and doping concentration were synthesized employing SILAR (Successive Ionic Layer Adsorption and Reaction) method previously reported.[21,50,117] The key control in the synthesis of Mn-doped CdS/ZnS core/shell NCs used in this study is the radial doping location of Mn^{2+} ions within the core/shell host NCs with lattice mismatch, which determines both the temperature sensitivity of Mn luminescence and its insensitivity to the surrounding chemical environment as discussed in detail in Results and Discussions. CdS core (3.6 nm) was prepared by injecting 1-octadecene (ODE) solution of sulfur to the mixture of cadmium oxide, ODE, and oleic acid at 250 °C. ZnS shell was coated using SILAR method by introducing the precursors of anion and cation alternately. ODE solution of sulfur and toluene solution of zinc stearate were used as the precursor of S and Zn respectively. The radial Mn doping location was controlled by introducing Mn precursor at different steps during the layer-by-layer coating of ZnS

shell. Oleylamine solution of Mn acetate or Mn diethyldithiocarbamate was used as the precursor of Mn. The details of the synthesis are provided in the Supporting Information.

5.4.2 Measurement of the Temperature-Dependent Mn Luminescence Spectra

Mn-doped CdS/ZnS NCs mixed with poly(methyl methacrylate) were spin-coated on the sapphire substrate. The temperature was controlled in an open-cycle cryostat (ST-100, Janis) using liquid nitrogen as the cryogen. The NCs on sapphire substrate were excited by a 403 nm *cw* diode laser at a low power (< 1 mW at 5 mm beam diameter). The luminescence spectra were measured with a fiber optic-coupled CCD spectrometer (QE65 Pro, Ocean Optics). A 450 nm long pass filter was used to block the scattered excitation light. The transmittance spectra of the two bandpass filters used for imaging (600 and 650 nm, 10 nm bandwidth) were used to obtain the temperature calibration curve from the measured Mn luminescence spectra.

5.4.3 Cryo-Cooling Device Fabrication

Figure V-5(a) illustrates the construction of the cryo-cooling device that provides a temperature gradient from 77-260 K over ~12 mm distance. Thin film of Mn-doped NCs was formed on a glass substrate from the solution of the NCs dispersed in chloroform via spin-coating. On top of the NCs-coated glass substrate, 15 μm-thick poly(dimethylsiloxane) (PDMS) layer was spin-coated and cured. The black PDMS substrate having a channel for the liquid nitrogen ($3\times3\times10$ mm^3, w×h×l) was replicated from a polymer master mold fabricated using a 3D printer (ULTRA, envision TEC).

Before applying the uncured black PDMS to the master mold, two silicon tubes were connected at the inlet and outlet port of the liquid nitrogen channel. The black PDMS was cured in an oven at 80 ºC for 1 hour and permanently bonded to the NCs- coated glass substrate. The device was placed in the enclosure made of black acetal resin blocks. The front of the enclosure has a glass window for the illumination and imaging purpose. The enclosure has the inlet and outlet port for the dry nitrogen gas used for flushing the interior of the enclosure.

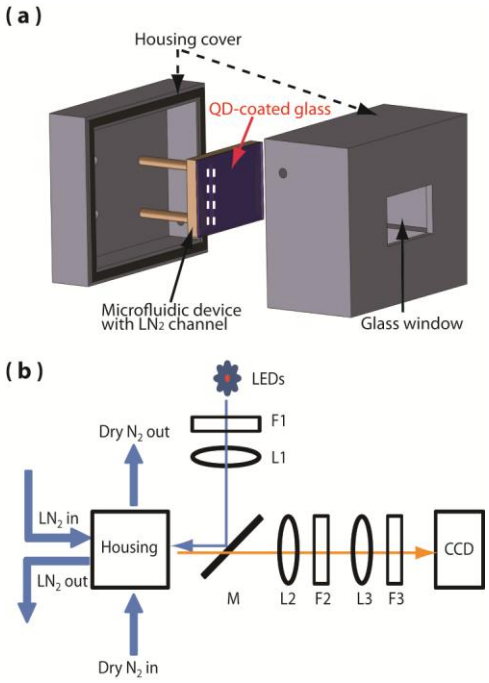

Figure V–5. Schematics of the cryo-cooling device, the enclosure and the temperature measurement setup. (a) The cryo-cooling device is in the enclosure in which dry nitrogen is constantly flushed. (b) The optical setup consists of filters (F), achromatic doublet lenses (L), and a dichroic mirror (M). The device was illuminated with a 365 nm LED and imaged with a CCD detector.

5.4.4 Surface Temperature Imaging of the Cyro-Cooling Device

The surface temperature profile of the cryo-cooling devices was measured with the setup shown in the Figure V-5(b). Liquid nitrogen flowing through the channel cooled the region of the glass substrate in contact with liquid nitrogen to 77 K. The dry nitrogen flow through the enclosure prevents frosting on the surface of the glass substrate and maintains the temperature gradient between 77 K and ambient temperature on the glass substrate. The cryo-cooling device was illuminated with a 365 nm UV LED and a collimating lens. 475 nm short-pass filter (F1) was placed after the LED to remove the red tail of the spectrum. A dichroic mirror (DMLP505R, Thorlabs) was used to reflect the excitation light from the LED and collect the luminescence from the device. A combination of an achromatic doublet lens (L2, focal length = 200 mm) and a microscope tube lens (L3, focal length = 200 mm) was used to image the surface of the device on the CCD camera (Princeton Instrument, PI-LCX) at 1X magnification. Temperature image was generated by taking the ratio of the two intensity images at 600 and 650 nm and using the calibration curve shown in Figure V-1(b). Each intensity image at 600 and 650 nm was separately recorded with 20 sec integration time by placing a bandpass filter (F3) in front of the CCD. With this setup, each pixel of CCD images 20x20 μm^2 area.

5.4.5 Finite Element Method Simulation

To simulate the temperature profile at the interface of glass and PDMS of the cryo-cooling device, finite element method (FEM) models were implemented using

Comsol Multiphysics™. Thermal conductivity parameters of 0.18 W mK^{-1} and 1.38 W mK^{-1} were selected for PDMS and glass, respectively. The temperature of the liquid nitrogen channel inside the PDMS block was set as 77 K. Outside boundary of the glass substrate had the heat flux with the heat transfer coefficient of 40 W $m^{-2}K^{-1}$. A forced convection was assumed to account for the dry nitrogen gas flow over the device.

CHAPTER VI

SUMMARY

As many semiconducting materials have expanded its electrical, optical, and magnetic properties with doping, doped quantum dots (QDs) have also attracted attention for introducing additional optical, electrical, magneto-optical properties. In the recent past two decades, tremendous efforts were invested to develop synthetic doping methods and characterize the intriguing properties in the doped QDs. Especially, recent development in synthetic routes for the Mn-doped CdS/ZnS QDs as a model system was attracted significant attention for their fascinating optical properties. Among those optical properties, the most interesting feature is mainly attributed to the energy transfer between the exciton and dopant, which depends on the energetics of exciton (donor) and dopant (acceptor) in the nanocrystals. In addition, development of the structural modification of the Mn-doped CdS/ZnS QDs such as controlling the radial doping location in the nanocrystals can induce photostability and highly efficient dopant luminescence (QY ≈ 80%), which arises from the fast energy transfer and localized nature of the ligand-field transition. Furthermore, the tunable temperature dependence of the Mn luminescence spectrum in Mn-doped CdS/ZnS QDs can make it possible for the doped nanocrystals to be utilized in the application field such as thermal sensing due to their significant temperature-dependent dopant luminescence via the optical tuning. For these reasons, considered as an important class of luminescent new nanomaterials, Mn-doped CdS/ZnS QDs was studied to show more efficient plasmonic luminescence

enhancement than typical luminophores and demonstrate application of the temperature-dependent Mn luminescence to a nanothermometer.

In the first project, the sensitized Mn luminescence, which arises from the fast exciton-dopant energy transfer occurring on a few ps time scale, exhibits a stronger plasmon-enhancement of luminescence than the exciton due to a suppression of MNP-induced quenching of the luminescence. The rapid energy transfer that separates the absorber (exciton) and emitter (Mn) in time can partially separate the plasmon-enhancement of the excitation from the MNP-induced quenching processes, both of which results from the presence of the plasmonic MNPs. When combined with the reduced spectral overlap between the sensitized Mn luminescence and MNP plasmon, as compared to the exciton luminescence, the Mn luminescence in Mn-doped QDs exhibited a stronger net plasmon enhancement than the exciton at the optimum separation between the MNP and QD layers. This study demonstrates that materials exhibiting fast sensitized luminescence that is sufficiently red-shifted from that of the sensitizer can be superior to usual luminophores in harvesting plasmon enhancement of luminescence by suppressing quenching.

In the second project, the sensitized Mn luminescence, which is highly insensitive to the surrounding chemical environments, was shown to demonstrate the ratiometric temperature imaging based on temperature-dependent Mn luminescence spectrum from Mn-doped CdS/ZnS QDs exhibiting near-linear temperature response in a broad range of temperatures (100−380 K). The Mn luminescence from the QDs used in this study was made highly insensitive to the variation of the surrounding chemical

environment, such as the surface passivation, polarity and pH of medium, by confining Mn^{2+} ions below the shell in core/shell structure of the QDs. The temperature sensitivity of the spectrum was enhanced by utilizing the local lattice strain created by the core/shell lattice mismatch that results in the stronger bandwidth broadening and peak shift with the temperature increase. Taking advantage of the weak environmental sensitivity of Mn luminescence spectrum and large temperature sensing range, the ratiometric temperature imaging of a cryo-cooling device was demonstrated. The surface temperature profile of the device ranging from 77 to 260 K was readily imaged with a CCD camera from the luminescence of the NCs spin-coated on the surface of the substrate. The method shown here will be particularly useful for the temperature imaging of the surfaces exhibiting a wide range of temperature variation and exposed to the chemically inhomogeneous environment.

REFERENCES

(1) Rossetti, R.; Nakahara, S.; Brus, L. E. *J. Chem. Phys* **1983**, *79*, 1086.

(2) Alivisatos, A. P. *Science* **1996**, *271*, 933.

(3) Nirmal, M.; Brus, L. *Acc. Chem. Res.* **1998**, *32*, 407.

(4) Murray, C. B.; Kagan, C. R.; Bawendi, M. G. *Annu. Rev. Mater. Sci.* **2000**, *30*, 545.

(5) Kim, J. Y.; Voznyy, O.; Zhitomirsky, D.; Sargent, E. H. *Adv. Mater.* **2013**, *25*, 4986.

(6) Reed, M. A.; Randall, J. N.; Aggarwal, R. J.; Matyi, R. J.; Moore, T. M.; Wetsel, A. E. *Phys. Rev. Lett.* **1988**, *60*, 535.

(7) El-Sayed, M. A. *Acc. Chem. Res.* **2004**, *37*, 326.

(8) Shirasaki, Y.; Supran, G. J.; Bawendi, M. G.; Bulovic, V. *Nature Photon.* **2013**, *7*, 13.

(9) Michalet, X.; Pinaud, F. F.; Bentolila, L. A.; Tsay, J. M.; Doose, S.; Li, J. J.; Sundaresan, G.; Wu, A. M.; Gambhir, S. S.; Weiss, S. *Science* **2005**, *307*, 538.

(10) Chan, W. C. W.; Maxwell, D. J.; Gao, X.; Bailey, R. E.; Han, M.; Nie, S. *Curr. Opin. Biotechnol.* **2002**, *13*, 40.

(11) McLaurin, E. J.; Bradshaw, L. R.; Gamelin, D. R. *Chem. Mater.* **2013**, *25*, 1283.

(12) Huynh, W. U.; Peng, X.; Alivisatos, A. P. *Adv. Mater.* **1999**, *11*, 923.

(13) Robel, I.; Subramanian, V.; Kuno, M.; Kamat, P. V. *J. Am. Chem. Soc.* **2006**, *128*, 2385.

(14) Talapin, D. V.; Murray, C. B. *Science* **2005**, *310*, 86.

(15) Erwin, S. C.; Zu, L.; Haftel, M. I.; Efros, A. L.; Kennedy, T. A.; Norris, D. J. *Nature* **2005**, *436*, 91.

(16) Norris, D. J.; Efros, A. L.; Erwin, S. C. *Science* **2008**, *319*, 1776.

(17) Beaulac, R.; Schneider, L.; Archer, P. I.; Bacher, G.; Gamelin, D. R. *Science* **2009**, *325*, 973.

(18) Mocatta, D.; Cohen, G.; Schattner, J.; Millo, O.; Rabani, E.; Banin, U. *Science* **2011**, *332*, 77.

(19) Norris, D. J.; Yao, N.; Charnock, F. T.; Kennedy, T. A. *Nano Lett.* **2000**, *1*, 3.

(20) Pradhan, N.; Goorskey, D.; Thessing, J.; Peng, X. *J. Am. Chem. Soc.* **2005**, *127*, 17586.

(21) Yang, Y.; Chen, O.; Angerhofer, A.; Cao, Y. C. *J. Am. Chem. Soc.* **2006**, *128*, 12428.

(22) Son, D. H.; Hughes, S. M.; Yin, Y.; Paul Alivisatos, A. *Science* **2004**, *306*, 1009.

(23) Beaulac, R.; Archer, P. I.; Gamelin, D. R. *J. Solid State Chem.* **2008**, *181*, 1582.

(24) Pradhan, N.; Sarma, D. D. *J. Phys. Chem. Lett.* **2011**, *2*, 2818.

(25) Chen, H.-Y.; Son, D. H. *Isr. J. Chem.* **2012**, *52*, 1016.

(26) Chen, H.-Y.; Maiti, S.; Nelson, C. A.; Zhu, X.; Son, D. H. *J. Phys. Chem. C* **2012**, *116*, 23838.

(27) Kelly, K. L.; Coronado, E.; Zhao, L. L.; Schatz, G. C. *J. Phys. Chem. B* **2002**, *107*, 668.

(28) Jain, P.; Huang, X.; El-Sayed, I.; El-Sayed, M. *Plasmonics* **2007**, *2*, 107.

(29) Ming, T.; Chen, H.; Jiang, R.; Li, Q.; Wang, J. *J. Phys. Chem. Lett.* **2011**, *3*, 191.

(30) Kosako, T.; Kadoya, Y.; Hofmann, H. F. *Nature Photon.* **2010**, *4*, 312.

(31) Shegai, T.; Li, Z.; Dadosh, T.; Zhang, Z.; Xu, H.; Haran, G. *Proc. Natl. Acad. Sci.* **2008**, *105*, 16448.

(32) Atwater, H. A.; Polman, A. *Nature Mater.* **2010**, *9*, 205.

(33) Haes, A. J.; Haynes, C. L.; McFarland, A. D.; Schatz, G. C.; Van Duyne, R. P.; Zou, S. *MRS Bull.* **2005**, *30*, 368.

(34) Jain, P. K.; Huang, X.; El-Sayed, I. H.; El-Sayed, M. A. *Acc. Chem. Res.* **2008**, *41*, 1578.

(35) Mayer, K. M.; Hafner, J. H. *Chem. Rev.* **2011**, *111*, 3828.

(36) Vuckovic, J.; Loncar, M.; Scherer, A. *IEEE J. Quant. Electron.* **2000**, *36*, 1131.

(37) Halas, N. J.; Lal, S.; Chang, W.-S.; Link, S.; Nordlander, P. *Chem. Rev.* **2011**, *111*, 3913.

(38) Daniel, M.-C.; Astruc, D. *Chem. Rev.* **2003**, *104*, 293.

(39) Jones, M. R.; Osberg, K. D.; Macfarlane, R. J.; Langille, M. R.; Mirkin, C. A. *Chem. Rev.* **2011**, *111*, 3736.

(40) Rycenga, M.; Cobley, C. M.; Zeng, J.; Li, W.; Moran, C. H.; Zhang, Q.; Qin, D.; Xia, Y. *Chem. Rev.* **2011**, *111*, 3669.

(41) Dulkeith, E.; Morteani, A. C.; Niedereichholz, T.; Klar, T. A.; Feldmann, J.; Levi, S. A.; van Veggel, F. C. J. M.; Reinhoudt, D. N.; Möller, M.; Gittins, D. I. *Phys. Rev. Lett.* **2002**, *89*, 203002.

(42) Soller, T.; Ringler, M.; Wunderlich, M.; Klar, T. A.; Feldmann, J.; Josel, H. P.; Markert, Y.; Nichtl, A.; Kürzinger, K. *Nano Lett.* **2007**, *7*, 1941.

(43) Eichelbaum, M.; Rademann, K. *Adv. Funct. Mater.* **2009**, *19*, 2045.

(44) Viste, P.; Plain, J.; Jaffiol, R.; Vial, A.; Adam, P. M.; Royer, P. *ACS Nano* **2010**, *4*, 759.

(45) Govorov, A. O.; Bryant, G. W.; Zhang, W.; Skeini, T.; Lee, J.; Kotov, N. A.; Slocik, J. M.; Naik, R. R. *Nano Lett.* **2006**, *6*, 984.

(46) Kulakovich, O.; Strekal, N.; Yaroshevich, A.; Maskevich, S.; Gaponenko, S.; Nabiev, I.; Woggon, U.; Artemyev, M. *Nano Lett.* **2002**, *2*, 1449.

(47) Pillonnet, A.; Berthelot, A.; Pereira, A.; Benamara, O.; Derom, S.; Francs, G. C. d.; Jurdyc, A.-M. *Appl. Phys. Lett.* **2012**, *100*, 153115.

(48) Park, Y.; Pravitasari, A.; Raymond, J. E.; Batteas, J. D.; Son, D. H. *ACS Nano* **2013**, *7*, 10544.

(49) Chen, H.-Y.; Chen, T.-Y.; Son, D. H. *J. Phys. Chem. C* **2010**, *114*, 4418.

(50) Chen, H.-Y.; Maiti, S.; Son, D. H. *ACS Nano* **2011**, *6*, 583.

(51) Fischer, L. H.; Harms, G. S.; Wolfbeis, O. S. *Angew. Chem. Int. Ed.* **2011**, *50*, 4546.

(52) Brites, C. D. S.; Lima, P. P.; Silva, N. J. O.; Millan, A.; Amaral, V. S.; Palacio, F.; Carlos, L. D. *Nanoscale* **2012**, *4*, 4799.

(53) Jaque, D.; Vetrone, F. *Nanoscale* **2012**, *4*, 4301.

(54) Walker, G. W.; Sundar, V. C.; Rudzinski, C. M.; Wun, A. W.; Bawendi, M. G.; Nocera, D. G. *Appl. Phys. Lett.* **2003**, *83*, 3555.

(55) Uchiyama, S.; Matsumura, Y.; de Silva, A. P.; Iwai, K. *Anal. Chem.* **2003**, *75*, 5926.

(56) Liebsch, G.; Klimant, I.; Wolfbeis, O. S. *Adv. Mater.* **1999**, *11*, 1296.

(57) Singh, S. K.; Kumar, K.; Rai, S. B. *Sens. Actuators, A* **2009**, *149*, 16.

(58) Brites, C. D. S.; Lima, P. P.; Silva, N. J. O.; Millán, A.; Amaral, V. S.; Palacio, F.; Carlos, L. D. *Adv. Mater.* **2010**, *22*, 4499.

(59) Cui, Y.; Xu, H.; Yue, Y.; Guo, Z.; Yu, J.; Chen, Z.; Gao, J.; Yang, Y.; Qian, G.; Chen, B. *J. Am. Chem. Soc.* **2012**, *134*, 3979.

(60) Vlaskin, V. A.; Janssen, N.; van Rijssel, J.; Beaulac, R. m.; Gamelin, D. R. *Nano Lett.* **2010**, *10*, 3670.

(61) Hsia, C.-H.; Wuttig, A.; Yang, H. *ACS Nano* **2011**, *5*, 9511.

(62) Ye, F.; Wu, C.; Jin, Y.; Chan, Y.-H.; Zhang, X.; Chiu, D. T. *J. Am. Chem. Soc.* **2011**, *133*, 8146.

(63) Reichardt, C. *Chem. Rev.* **1994**, *94*, 2319.

(64) Zohar, O.; Ikeda, M.; Shinagawa, H.; Inoue, H.; Nakamura, H.; Elbaum, D.; Alkon, D. L.; Yoshioka, T. *Biophys. J.* **1998**, *74*, 82.

(65) Parker, D. *Coord. Chem. Rev.* **2000**, *205*, 109.

(66) Park, Y.; Koo, C.; Chen, H.-Y.; Han, A.; Son, D. H. *Nanoscale* **2013**, *5*, 4944.

(67) Bhargava, R. N.; Gallagher, D.; Hong, X.; Nurmikko, A. *Phys. Rev. Lett.* **1994**, *72*, 416.

(68) CB, M.; DJ, N.; MG, B. *J. Am. Chem. Soc.* **1993**, *115*, 8706.

(69) Dalpian, G. M.; Chelikowsky, J. R. *Phys. Rev. Lett.* **2006**, *96*, 226802.

(70) Beaulac, R.; Archer, P. I.; Ochsenbein, S. T.; Gamelin, D. R. *Adv. Funct. Mater.* **2008**, *18*, 3873.

(71) Knowles, K. E.; McArthur, E. A.; Weiss, E. A. *ACS Nano* **2011**, *5*, 2026.

(72) Maiti, S.; Chen, H.-Y.; Park, Y.; Son, D. H. *J. Phys. Chem. C* **2014**, *118*, 18226.

(73) Beaulac, R.; Archer, P. I.; Ochsenbein, S. T.; Gamelin, D. R. *Adv. Funct. Mater.* **2008**, *18*, 3873.

(74) Pierres, A.; Benoliel, A. M.; Bongrand, P.; Ronda, C. R.; Amrein, T. *J. Lumin.* **1996**, *69*, 245.

(75) Zuo, T.; Sun, Z.; Zhao, Y.; Jiang, X.; Gao, X. *J. Am. Chem. Soc.* **2010**, *132*, 6618.

(76) Ithurria, S.; Guyot-Sionnest, P.; Mahler, B.; Dubertret, B. *Phys. Rev. Lett.* **2007**, *99*, 265501.

(77) Chan, Y.-H.; Chen, J.; Wark, S. E.; Skiles, S. L.; Son, D. H.; Batteas, J. D. *ACS Nano* **2009**, *3*, 1735.

(78) Yun, C. S.; Javier, A.; Jennings, T.; Fisher, M.; Hira, S.; Peterson, S.; Hopkins, B.; Reich, N. O.; Strouse, G. F. *J. Am. Chem. Soc.* **2005**, *127*, 3115.

(79) Pons, T.; Medintz, I. L.; Sapsford, K. E.; Higashiya, S.; Grimes, A. F.; English, D. S.; Mattoussi, H. *Nano Lett.* **2007**, *7*, 3157.

(80) Govorov, A. O.; Lee, J.; Kotov, N. A. *Phys. Rev. B* **2007**, *76*, 125308.

(81) Mao, H.; Yang, T.; Cremer, P. S. *J. Am. Chem. Soc.* **2002**, *124*, 4432.

(82) Graham, E. M.; Iwai, K.; Uchiyama, S.; Prasanna de Silva, A.; Magennis, S. W.; Jones, A. C. *Lab Chip* **2010**, *10*, 1267.

(83) Sadat, S.; Tan, A.; Chua, Y. J.; Reddy, P. *Nano Lett.* **2010**, *10*, 2613.

(84) Gota, C.; Okabe, K.; Funatsu, T.; Harada, Y.; Uchiyama, S. *J. Am. Chem. Soc.* **2009**, *131*, 2766.

(85) Yang, J.-M.; Yang, H.; Lin, L. *ACS Nano* **2011**, *5*, 5067.

(86) Okabe, K.; Inada, N.; Gota, C.; Harada, Y.; Funatsu, T.; Uchiyama, S. *Nat. Commun.* **2012**, *3*, 705.

(87) Bullen, C.; Mulvaney, P. *Langmuir* **2006**, *22*, 3007.

(88) Liu, Y.-S.; Sun, Y.; Vernier, P. T.; Liang, C.-H.; Chong, S. Y. C.; Gundersen, M. A. *J. Phys. Chem. C* **2007**, *111*, 2872.

(89) Kagan, C. R.; Murray, C. B.; Nirmal, M.; Bawendi, M. G. *Phys. Rev. Lett.* **1996**, *76*, 1517.

(90) Wuister, S. F.; de Mello Donegá, C.; Meijerink, A. *J. Phys. Chem. B* **2004**, *108*, 17393.

(91) van Sark, W. G. J. H. M.; Frederix, P. L. T. M.; Van den Heuvel, D. J.; Gerritsen, H. C.; Bol, A. A.; van Lingen, J. N. J.; de Mello Donegá, C.; Meijerink, A. *J. Phys. Chem. B* **2001**, *105*, 8281.

(92) Saada, A. S. *Elasticity Theory and Applications*, 1993.

(93) Rockenberger, J.; Troger, L.; Rogach, A. L.; Tischer, M.; Grundmann, M.; Eychmuller, A.; Weller, H. *J. Chem. Phys.* **1998**, *108*, 7807.

(94) Chen, W.; Sammynaiken, R.; Huang, Y.; Malm, J. O.; Wallenberg, R.; Bovin, J. O.; Zwiller, V.; Kotov, N. A. *J. Appl. Phys.* **2001**, *89*, 1120.

(95) Suyver, J. F.; Kelly, J. J.; Meijerink, A. *J. Lumin.* **2003**, *104*, 187.

(96) MacKay, J. F.; Becker, W. M.; Spaek, J.; Debska, U. *Phys. Rev. B* **1990**, *42*, 1743.

(97) Li, H.; Zhang, J.; Zhou, X.; Lu, G.; Yin, Z.; Li, G.; Wu, T.; Boey, F.; Venkatraman, S. S.; Zhang, H. *Langmuir* **2009**, *26*, 5603.

(98) Govorov, A. O.; Bryant, G. W.; Zhang, W.; Skeini, T.; Lee, J.; Kotov, N. A.; Slocik, J. M.; Naik, R. R. *Nano Lett.* **2006**, *6*, 984.

(99) Ni, W.; Ambjörnsson, T.; Apell, S. P.; Chen, H.; Wang, J. *Nano Lett.* **2009**, *10*, 77.

(100) Achermann, M. *J. Phys. Chem. Lett.* **2010**, *1*, 2837.

(101) Saboktakin, M.; Ye, X.; Oh, S. J.; Hong, S.-H.; Fafarman, A. T.; Chettiar, U. K.; Engheta, N.; Murray, C. B.; Kagan, C. R. *ACS Nano* **2012**, *6*, 8758.

(102) Yates, C. J.; Samuel, I. D. W.; Burn, P. L.; Wedge, S.; Barnes, W. L. *Appl. Phys. Lett.* **2006**, *88*, 161105.

(103) Choulis, S. A.; Mathai, M. K.; Choong, V.-E. *Appl. Phys. Lett.* **2006**, *88*, 213503.

(104) Kwon, M.-K.; Kim, J.-Y.; Kim, B.-H.; Park, I.-K.; Cho, C.-Y.; Byeon, C. C.; Park, S.-J. *Adv. Mater.* **2008**, *20*, 1253.

(105) Chen, Y.; Munechika, K.; Plante, I. J.-L.; Munro, A. M.; Skrabalak, S. E.; Xia, Y.; Ginger, D. S. *Appl. Phys. Lett.* **2008**, *93*, 053106.

(106) Munechika, K.; Chen, Y.; Tillack, A. F.; Kulkarni, A. P.; Plante, I. J.-L.; Munro, A. M.; Ginger, D. S. *Nano Lett.* **2010**, *10*, 2598.

(107) Carminati, R.; Greffet, J. J.; Henkel, C.; Vigoureux, J. M. *Opt. Commun.* **2006**, *261*, 368.

(108) Valeur, B. In *Molecular Fluorescence*; Wiley-VCH Verlag GmbH: 2001, p 72.

(109) Persson, B. N. J.; Lang, N. D. *Phys. Rev. B* **1982**, *26*, 5409.

(110) Pradhan, N.; Battaglia, D. M.; Liu, Y.; Peng, X. *Nano Lett.* **2006**, *7*, 312.

(111) Kagan, C. R.; Murray, C. B.; Bawendi, M. G. *Phys. Rev. B* **1996**, *54*, 8633.

(112) Komarala, V. K.; Bradley, A. L.; Rakovich, Y. P.; Byrne, S. J.; Gun'ko, Y. K.; Rogach, A. L. *Appl. Phys. Lett.* **2008**, *93*, 123102.

(113) Rogach, A. L.; Klar, T. A.; Lupton, J. M.; Meijerink, A.; Feldmann, J. *J. Mater. Chem.* **2009**, *19*, 1208.

(114) Crooker, S. A.; Hollingsworth, J. A.; Tretiak, S.; Klimov, V. I. *Phys. Rev. Lett.* **2002**, *89*, 186802.

(115) White, M. A.; Weaver, A. L.; Beaulac, R.; Gamelin, D. R. *ACS Nano* **2011**, *5*, 4158.

(116) Lakowicz, J. R. *Principles of fluorescence spectroscopy*; Springer, 2009.

(117) Yu, W. W.; Peng, X. *Angew. Chem. Int. Ed.* **2002**, *41*, 2368.

(118) Maciel, G. S.; Alencar, M.; rcio, A. R. C.; de, A.; jo, C. B.; Patra, A. *J. Nanosci. Nanotechnol.* **2010**, *10*, 2143.

(119) Oyama, K.; Takabayashi, M.; Takei, Y.; Arai, S.; Takeoka, S.; Ishiwata, S. i.; Suzuki, M. *Lab on a Chip* **2012**, *12*, 1591.

(120) Chen, D.; Viswanatha, R.; Ong, G. L.; Xie, R.; Balasubramaninan, M.; Peng, X. *J. Am. Chem. Soc.* **2009**, *131*, 9333.

(121) Zheng, J.; Ji, W.; Wang, X.; Ikezawa, M.; Jing, P.; Liu, X.; Li, H.; Zhao, J.; Masumoto, Y. *J. Phys. Chem. C* **2010**, *114*, 15331.

(122) Maestro, L. M.; Rodríguez, E. M. n.; Rodríguez, F. S.; la Cruz, M. C. I.-d.; Juarranz, A.; Naccache, R.; Vetrone, F.; Jaque, D.; Capobianco, J. A.; Solé, J. G. a. *Nano Lett.* **2010**, *10*, 5109.

(123) Vetrone, F.; Naccache, R.; Zamarrón, A.; Juarranz de la Fuente, A.; Sanz-Rodríguez, F.; Martinez Maestro, L.; Martín Rodriguez, E.; Jaque, D.; García Solé, J.; Capobianco, J. A. *ACS Nano* **2010**, *4*, 3254.

(124) Larsen, B. A.; Deria, P.; Holt, J. M.; Stanton, I. N.; Heben, M. J.; Therien, M. J.; Blackburn, J. L. *J. Am. Chem. Soc.* **2012**, *134*, 12485.

(125) Williams, K. J.; Tisdale, W. A.; Leschkies, K. S.; Haugstad, G.; Norris, D. J.; Aydil, E. S.; Zhu, X. Y. *ACS Nano* **2009**, *3*, 1532.

(126) Law, M.; Luther, J. M.; Song, Q.; Hughes, B. K.; Perkins, C. L.; Nozik, A. J. *J. Am. Chem. Soc.* **2008**, *130*, 5974.

(127) Koo, C.; Godley, R. F.; Park, J.; McDougall, M. P.; Wright, S. M.; Han, A. *Lab on a Chip* **2011**, *11*, 2197.